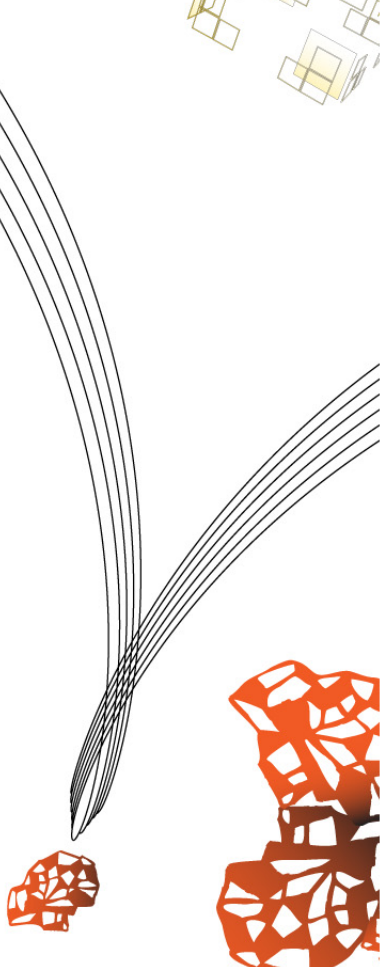
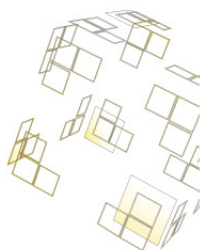


Master's thesis Applied Mathematics

(Chair: Applied Analysis and Computational Science, Track: Multiscale Modeling and Simulation)

Faculty of Electrical Engineering, Mathematics and Computer Science (EEMCS)

# Large Eddy Simulation of Interfacial Gas-Liquid Turbulent Channel Flow



Jorn Lucas (s0173398)

**Assessment Committee:**

Prof. Dr. Ir. B.J. Geurts (UT)

Dr. M. Botchev (UT)

Dr. A. Zagaris (UT)

**Supervisors:**

Prof. Dr. V. Armenio (UniTS)

Prof. Dr. Ir. B.J. Geurts (UT)

December 12, 2013

**UNIVERSITY OF TWENTE.**



UNIVERSITÀ  
DEGLI STUDI DI TRIESTE



# Contents

<b>1 Problem</b>	<b>5</b>
<b>2 Literature</b>	<b>7</b>
<b>3 Analysis</b>	<b>9</b>
<b>4 Interface Boundary Conditions</b>	<b>11</b>
<b>5 One-Dimensional Verification</b>	<b>13</b>
<b>6 Boundary Reynolds Number</b>	<b>25</b>
<b>7 Three-Dimensional Setup</b>	<b>27</b>
<b>8 Results</b>	<b>29</b>
8.1 Quadrant Analysis . . . . .	37
8.2 Turbulence . . . . .	50
<b>9 Conclusion</b>	<b>53</b>
<b>10 Discussion</b>	<b>55</b>
<b>A Notation</b>	<b>III</b>
<b>B Spatial and Temporal Correlation</b>	<b>VII</b>
<b>C Turbulence Statistics</b>	<b>IX</b>
<b>D Turbulent Kinetic Energy</b>	<b>XIII</b>



# CHAPTER 1

## PROBLEM

---

Fluid flows affect every part of life, from the water flowing from your tap to the weather outside. Understanding these fluid flows at all scales is therefore an important goal of science. At the Department for Industrial and Environmental Fluid Mechanics, based in the Università degli Studi di Trieste, they perform a lot of research in understanding and modelling fluid flows.

To do this, the Navier-Stokes equations which describe the behaviour of fluids, have been modelled using large eddy simulation (LES). This program works accurately and has been applied to both theoretical and practical flows.

The outset of this thesis is to find if and how this LES model can be applied to simulating the interaction between two fluids.

Previous research in this area will be discussed in Section 2, Literature. A theoretical foundation is laid by solving the Navier-Stokes equations analytically in one dimension for one and two fluids in Section 3, Analysis.

From this theory and the previous research, the boundary conditions at the interface are adapted to work with the LES-model in Section 4. Finally, the boundary conditions are verified by comparing the results of the LES-model in one dimension with the analytical solution in Section 5.

To apply this model to a meaningful three-dimensional flow, more analysis is performed on the characteristics of the desired flows in Section 6. The model is then applied to a flow of two immiscible fluids, with the same relation between them as water and air, in a plane channel. The results are available in Section 8.

There, the characteristics of this flow will be carefully described, as well as compared to similar research. Special attention is given to the behaviour of the turbulence near the interface.

Details about the notation, statistics and formulas used for describing these characteristics can be found in the Appendix.



## CHAPTER 2

# LITERATURE

---

The present work has been done using an LES-model based on the fractional-step algorithm proposed by Zang et. al, [10], which has been expanded and verified to be second-order accurate in time and space by Armenio and Piomelli, [2].

The applicability of such a model to the simulation of complex two-dimensional and three-dimensional flow fields has been well-documented. Two-dimensional flows like a lid-driven cavity and a backward facing step (Kim and Moin, [5]) have been successfully simulated by a model which can be seen as a precursor to Zang et al, [10]. Also a three-dimensional plane channel flow with one fluid has been simulated with the same model, by Kim, Moin and Moser, [6]. Their results have been compared to previous researches, showing very good agreement between both experimental and numerical findings. Therefore, this model is applicable in modelling the viscous coupling of two fluids at low Reynolds numbers.

The modelling of two fluids started with single fluids with a free surface without much deformation. These results did not significantly differ from viscous coupling without any deformation, see Lam and Banerjee, [7]. Two-fluid simulations have then focused on low Reynolds number flows, namely Lombardi et al, [8], similar to what has been done in this thesis, but with opposite pressure gradients for both fluids. Their conclusion was that shear is the most important in determining the dominant flow structure near the interface (Lam, Banerjee 1992 if I can find it) and that these caused streaklike structures, especially sweeps in high-shear areas and ejections in low-shear areas above the interface (Lombardi et al., [8]).

Experimental research by Ansari and Arzandi, [1], shows the behaviour of the interface between air and water in a duct, a plane channel bounded by walls. One of these is stratified flow, which has been assumed here for ease of simulation purposes.

More recently, deformable interfaces have also been incorporated into some models, like Fulgosi et al., [3], and Yang and Shen, [9], but an extension of such methods to the used LES-model is not yet available.



## CHAPTER 3

# ANALYSIS

---

The task is to numerically solve the incompressible Navier-Stokes equations. These are given by the continuity equation:

$$\frac{\partial u_j}{\partial x_j} = 0 \quad (3.1)$$

And the Navier-Stokes equations:

$$\frac{\partial u_i}{\partial t} + \frac{\partial (u_j u_i)}{\partial x_j} = -\frac{\partial p}{\partial x_i} + \nu \frac{\partial^2 u_i}{\partial x_j^2} \quad (3.2)$$

In both cases, the Einstein summation convention applies. Indices  $i$  and  $j$  refer to the direction. Simplifying these equations into one dimension yields:

$$\frac{\partial u}{\partial x} = 0 \quad (3.3)$$

$$\frac{\partial u}{\partial t} + \frac{\partial}{\partial x} u^2 = -\frac{\partial p}{\partial x} + \nu \frac{\partial^2 u}{\partial x^2} \quad (3.4)$$

Now, the assumption is that the pressure gradient is constant. Also, due to the fact that equation (3.3) only allows for constant solutions in the one-dimensional case, this equation is reserved for multi-dimensional Navier-Stokes equations.

The discretisation is done using Adams-Bashforth on the convective term  $(\frac{\partial}{\partial x} u^2)$  and Crank-Nicolson on the viscous term  $(\nu \frac{\partial^2 u}{\partial x^2})$ . This leads to a semi-implicit time advancement scheme. An alternative method available is also applying an explicit Adams-Bashforth scheme to the viscous terms.

The discretisation for the fully explicit scheme then becomes:

$$\begin{aligned} \frac{u_k^{n+1} - u_k^n}{\Delta t} = & \frac{3}{2} \left( -\frac{(u_{k+1}^n)^2 - (u_{k-1}^n)^2}{2\Delta x} - \frac{\partial p}{\partial x} + \nu \frac{u_{k+1}^n - 2u_k^n + u_{k-1}^n}{(\Delta x)^2} \right) \\ & - \frac{1}{2} \left( -\frac{(u_{k+1}^{n-1})^2 - (u_{k-1}^{n-1})^2}{2\Delta x} - \frac{\partial p}{\partial x} + \nu \frac{u_{k+1}^{n-1} - 2u_k^{n-1} + u_{k-1}^{n-1}}{(\Delta x)^2} \right) \end{aligned} \quad (3.5)$$

And for the semi-implicit scheme:

$$\begin{aligned} \frac{u_k^{n+1} - u_k^n}{\Delta t} = & \frac{3}{2} \left( -\frac{(u_{k+1}^n)^2 - (u_{k-1}^n)^2}{2\Delta x} - \frac{\partial p}{\partial x} \right) \\ & - \frac{1}{2} \left( -\frac{(u_{k+1}^{n-1})^2 - (u_{k-1}^{n-1})^2}{2\Delta x} - \frac{\partial p}{\partial x} \right) \\ & + \frac{1}{2} \nu \frac{u_{k+1}^n - 2u_k^n + u_{k-1}^n}{(\Delta x)^2} + \frac{1}{2} \nu \frac{u_{k+1}^{n+1} - 2u_k^{n+1} + u_{k-1}^{n+1}}{(\Delta x)^2} \end{aligned} \quad (3.6)$$

Now, to apply a fractional-step algorithm, there is need for a predictor and a corrector. Therefore, the off-diagonal terms will be treated explicitly, making from 3.6:

$$\begin{aligned} \frac{u_k^{n+1} - u_k^n}{\Delta t} \left( 1 + \frac{\nu \Delta t}{(\Delta x)^2} \right) &= \frac{3}{2} \left( -\frac{(u_{k+1}^n)^2 - (u_{k-1}^n)^2}{2\Delta x} - \frac{\partial p}{\partial x} \right) \\ &\quad - \frac{1}{2} \left( -\frac{(u_{k+1}^{n-1})^2 - (u_{k-1}^{n-1})^2}{2\Delta x} - \frac{\partial p}{\partial x} \right) \\ &\quad + \nu \frac{u_{k+1}^n - 2u_k^n + u_{k-1}^n}{(\Delta x)^2} \end{aligned} \quad (3.7)$$

Which yields the prediction step:

$$\begin{aligned} \frac{u_k^* - u_k^n}{\Delta t} \left( 1 + \frac{\nu \Delta t}{(\Delta x)^2} \right) &= \frac{3}{2} \left( -\frac{(u_{k+1}^n)^2 - (u_{k-1}^n)^2}{\Delta x} \right) \\ &\quad - \frac{1}{2} \left( -\frac{(u_{k+1}^{n-1})^2 - (u_{k-1}^{n-1})^2}{\Delta x} \right) \\ &\quad + \nu \frac{u_{k+1}^n - 2u_k^n + u_{k-1}^n}{(\Delta x)^2} \end{aligned} \quad (3.8)$$

And the correction step:

$$\frac{u_k^{n+1} - u_k^*}{\Delta t} = -\frac{\partial p}{\partial x} \left( 1 + \frac{\nu \Delta t}{(\Delta x)^2} \right)^{-1} \quad (3.9)$$

The notable difference to the work in [10] is in the pressure gradient, for it is considered to be a constant in the LES model.

Using these discretization methods, simulating one fluid is completely possible and done successfully, for example in [2]. The goal of simulating the behaviour of two fluids on top of each other is within reach, by doubling all persistent variables in the model and programming it to switch between calculating one fluid and the other. The next step is to make these two fluids communicate at the interface.

## CHAPTER 4

# INTERFACE BOUNDARY CONDITIONS

---

For modelling the behaviour at an interface, a boundary condition suggested by literature ([8] and [4] for example) is to have continuous velocity and continuous shear stress at the interface. At the walls, the boundary condition is that the velocity is equal to zero. The interface is also assumed to be flat and at a constant height, similar to [8]. If both fluids have length two in the  $y$ -direction, then these are the boundary conditions at the interface:

$$u_1(2) = u_2(2) \quad (4.1)$$

$$v_1(2) = v_2(2) = 0 \quad (4.2)$$

$$w_1(2) = w_2(2) \quad (4.3)$$

$$\mu_1 \left. \frac{\partial u_1}{\partial y} \right|_{y=2} = \mu_2 \left. \frac{\partial u_2}{\partial y} \right|_{y=2} \quad (4.4)$$

$$\mu_1 \left. \frac{\partial w_1}{\partial y} \right|_{y=2} = \mu_2 \left. \frac{\partial w_2}{\partial y} \right|_{y=2} \quad (4.5)$$

The implementation of the first three conditions is straightforward. However, the last two require discretisation. Because the model used is second-order accurate, there is also the requirement for a second-order forward discretisation. Things are further complicated by the fact a stretched grid will be used in more complex simulations. Therefore, a general second-order boundary condition is derived for an arbitrarily spaced grid.

It is known that a second-order forward boundary condition should be of the following form.

$$\left. \frac{\partial u}{\partial y} \right|_{y=2} = au(2) + bu(2 + \Delta^1 y) + cu(2 + \Delta^2 y) + O(\Delta y^3) \quad (4.6)$$

With  $a$ ,  $b$  and  $c$  the unknowns and  $\Delta^1 y$  and  $\Delta^2 y$  the distance between grid points. Taking the Taylor expansions of the second and third term of the right part yields:

$$u(2 + \Delta^1 y) = u(2) + \Delta^1 y \left. \frac{\partial u}{\partial y} \right|_{y=2} + \frac{(\Delta^1 y)^2}{2} \left. \frac{\partial^2 u}{\partial y^2} \right|_{y=2} + O(\Delta y^3)$$

$$u(2 + \Delta^2 y) = u(2) + \Delta^2 y \left. \frac{\partial u}{\partial y} \right|_{y=2} + \frac{(\Delta^2 y)^2}{2} \left. \frac{\partial^2 u}{\partial y^2} \right|_{y=2} + O(\Delta y^3)$$

Filling this into (4.6) gives:

$$\left. \frac{\partial u}{\partial y} \right|_{y=2} = (a + b + c)u(2) + (\Delta^1 y b + \Delta^2 y c) \left. \frac{\partial u}{\partial y} \right|_{y=2} + \left( \frac{(\Delta^1 y)^2}{2} b + \frac{(\Delta^2 y)^2}{2} c \right) \left. \frac{\partial^2 u}{\partial y^2} \right|_{y=2} + O(\Delta y^3) \quad (4.7)$$

This is a system of equations that will be second-order when:

$$\begin{aligned} a + b + c &= 0 \\ \Delta^1 y b + \Delta^2 y c &= 1 \\ \frac{(\Delta^1 y)^2}{2} b + \frac{(\Delta^2 y)^2}{2} c &= 0 \end{aligned}$$

Solving this for  $a$ ,  $b$  and  $c$  results in:

$$a = -\frac{\Delta^1 y + \Delta^2 y}{\Delta^1 y \Delta^2 y} \quad (4.8)$$

$$b = -\frac{1}{\Delta^1 y \left( \frac{\Delta^1 y}{\Delta^2 y} - 1 \right)} \quad (4.9)$$

$$c = \frac{1}{\Delta^2 y \left( 1 - \frac{\Delta^2 y}{\Delta^1 y} \right)} \quad (4.10)$$

Expanding this to two grids of different size and then implementing (4.10) and the continuous velocity into the boundary condition for the shear stress (4.5), yields:

$$u_1(2) = u_2(2) = \frac{\mu_2 b_2 u(2 + \Delta_2^1 y) + \mu_2 c_2 u(2 + \Delta_2^2 y) - \mu_1 b_1 u(2 + \Delta_1^1 y) - \mu_1 c_1 u(2 + \Delta_1^2 y)}{\mu_1 a_1 - \mu_2 a_2} \quad (4.11)$$

with  $\Delta_1^1 y$  the distance for the top fluid at the first grid point from the interface,  $\Delta_1^2 y$  the distance for the top fluid at the second grid point from the interface. The distances  $\Delta_2^1 y$  and  $\Delta_2^2 y$  are negative, as well as the coefficients, for example  $a_2 = -a_1 = a$  from (4.10).

## CHAPTER 5

# ONE-DIMENSIONAL VERIFICATION

---

Verification of the one-dimensional model is paramount for increasing the scope of the model. If the technique mentioned in Section 4 works in one dimension, the first step in applying it to three dimensions is expanding this technique. Moreover, exact solutions are known for one dimension, providing a good basis for verification. The most simple of these is Couette flow. This is a shear-driven fluid motion, where two parallel plates are at a distance from each other and moving relatively to one another. Pressure gradients are neglected, reducing the one-dimensional Navier-Stokes equation to:

$$\begin{aligned}\frac{\partial u}{\partial t} &= \frac{\partial^2 u}{\partial y^2} & (5.1) \\ u(h_0) &= u_b \\ u(h_1) &= u_t\end{aligned}$$

With  $h_0$  and  $h_1$  the height of the bottom and the top of the domain respectively. The steady-state solution should have  $\partial u / \partial t = 0$ , resulting in:

$$\frac{\partial^2 u}{\partial y^2} = 0 \quad (5.2)$$

$$u(y) = \frac{u_t - u_b}{h_1 - h_0} y + \frac{u_b h_1 - u_t h_0}{h_1 - h_0} \quad (5.3)$$

Using the one-fluid model to simulate these conditions, with the height going from 0 to 4 and the upper plate velocity at 1 and the lower plate velocity at 0, the solution is the straight line in Fig. 5.1.

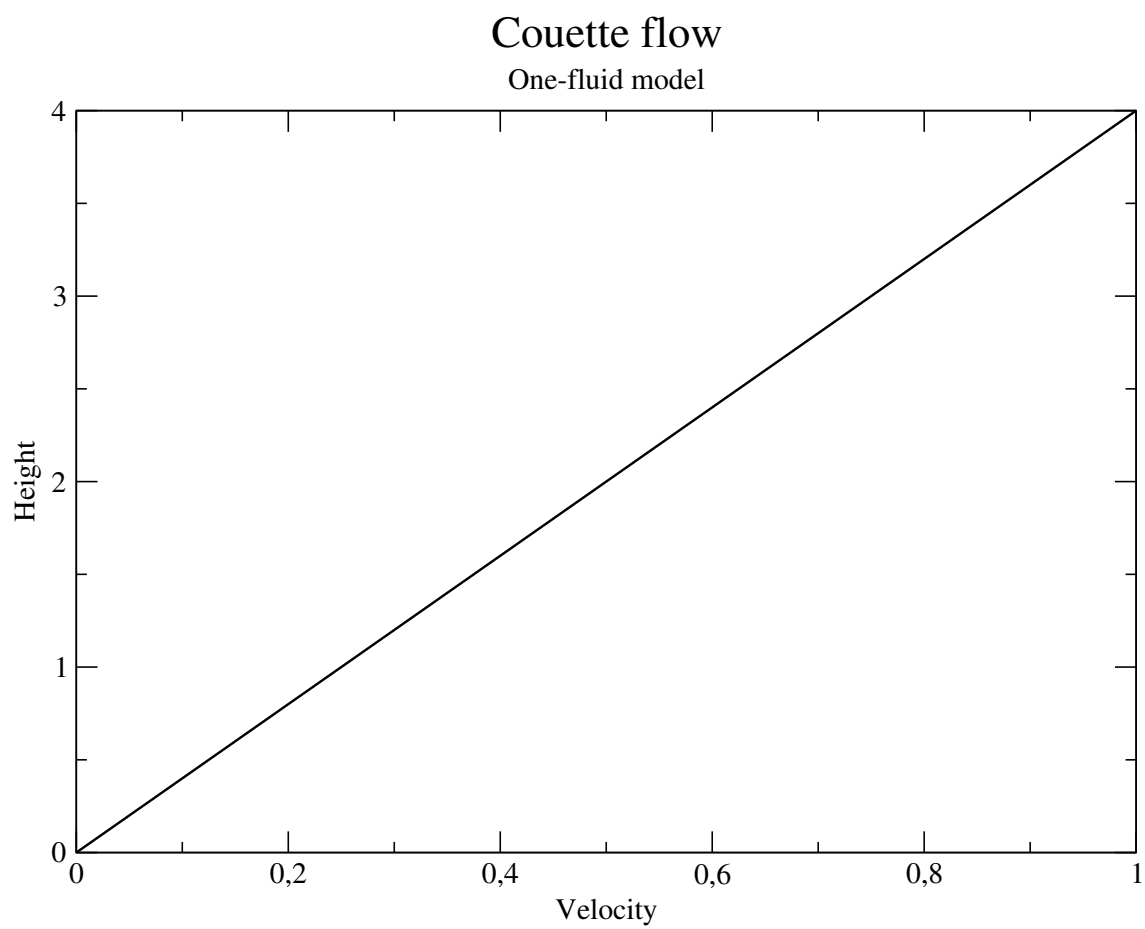


Fig. 5.1: Solution obtained by the one-fluid model for Couette flow

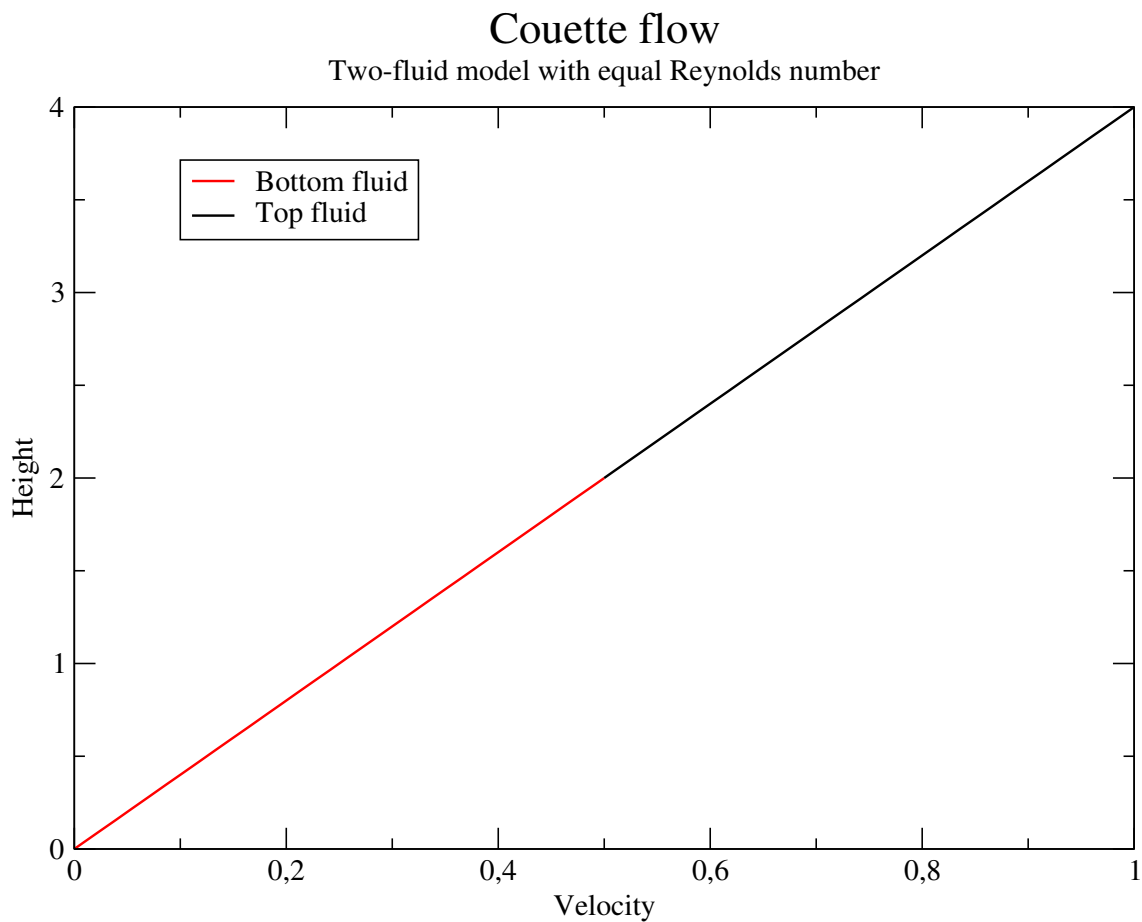


Fig. 5.2: Solution obtained by the two-fluid model for Couette flow

Using the two-fluid model with two fluids of the same viscosity, the same solution is obtained, as displayed in Fig. 5.2.

When one introduces a constant pressure gradient in this equation, the result is called plane Poiseuille flow. No velocity is present at either of the boundaries, so the pressure is the only thing driving the flow. The one-dimensional Navier-Stokes equations become:

$$\begin{aligned} \frac{\partial u}{\partial t} &= \frac{\partial^2 u}{\partial y^2} - \frac{1}{\mu} \frac{dp}{dx} \\ u(h_0) &= 0 \\ u(h_1) &= 0 \end{aligned} \quad (5.4)$$

With  $\mu$  the fluid viscosity. The steady-state solution is:

$$u(y) = \frac{1}{2\mu} \frac{dp}{dx} (y^2 - (h_1 + h_0)y + h_1 h_0) \quad (5.5)$$

Both the one-fluid model and the two-fluid model converge to this analytical solution, as can be seen in Fig. 5.3.

With these test cases, it is verified that the two-fluid model yields the same steady-state solutions as the one-fluid model does. A natural choice for a third test case is a system without a steady-state solution, for example the Stokes oscillating plate. This has a sinusoidal boundary condition and as such only has a cyclic solution at a steady state. One can now also observe whether the convergence to this cyclic state is affected by the boundary condition in the two-fluid model. Again, the pressure gradient is neglected, resulting in the equation:

$$\begin{aligned}\frac{\partial u}{\partial t} &= \frac{\partial^2 u}{\partial y^2} & (5.6) \\ u(h_0) &= 0 \\ u(h_1) &= A \sin(\omega t)\end{aligned}$$

With  $A$  the amplitude of the oscillation and  $\omega$  the frequency. For one fluid a steady cyclic solution is obtained after a startup (Fig. 5.4).

There is convergence to a certain repeating state. The two-fluid model exhibits the same behaviour. It is possible however, that the boundary conditions at the interface do not transmit information fast enough to keep up with the oscillation. Therefore, the different models have been compared at a height of  $y = 0.96875$ , just below the interface. The effects, Fig. 5.5, are negligible, leading to the conclusion that the two-fluid model possesses the robustness of the one-fluid model.

With the verification that the two-fluid model works, the step to two-fluid flows is made. For both Couette flow and Poiseuille flow, the analytical solution for two fluids is easily described and derived. To keep the equations clean,  $h_0$  and  $h_1$  have been replaced by 0 and 4 respectively. The interface is set at 2. For Couette flow, the equation now looks like:

$$\frac{\partial u_1}{\partial t} = \frac{\partial^2 u_1}{\partial y^2}, y \in (0, 2) \quad (5.7)$$

$$\frac{\partial u_2}{\partial t} = \frac{\partial^2 u_2}{\partial y^2}, y \in (2, 4) \quad (5.8)$$

$$u_1(0) = 0$$

$$u_1(2) = u_2(2)$$

$$u_2(4) = 1$$

$$\mu_1 \left. \frac{\partial u_1}{\partial y} \right|_{y=2} = \mu_2 \left. \frac{\partial u_2}{\partial y} \right|_{y=2}$$

The steady-state solution to this equation is:

$$u_1(y) = \frac{\mu_2}{2(\mu_1 + \mu_2)} y \quad (5.9)$$

$$u_2(y) = \frac{\mu_1}{2(\mu_1 + \mu_2)} y + \frac{\mu_2 - \mu_1}{\mu_1 + \mu_2} \quad (5.10)$$

As such, the expectation is that two straight lines, connected but at an angle, will be the steady-state solution of the program. In Fig. 5.6, this result is observed.

The description for the most basic two-fluid Poiseuille flow is:

$$\frac{\partial u_1}{\partial t} = \frac{\partial^2 u_1}{\partial y^2} - \frac{1}{\mu_1} \frac{dp}{dx}, y \in (0, 2) \quad (5.11)$$

$$\frac{\partial u_2}{\partial t} = \frac{\partial^2 u_2}{\partial y^2} - \frac{1}{\mu_2} \frac{dp}{dx}, y \in (2, 4) \quad (5.12)$$

$$u_1(0) = 0$$

$$u_1(2) = u_2(2)$$

$$u_2(4) = 0$$

$$\mu_1 \left. \frac{\partial u_1}{\partial y} \right|_{y=2} = \mu_2 \left. \frac{\partial u_2}{\partial y} \right|_{y=2}$$

Because  $dp/dx$  is a constant, replacing it by unity will not change the shape of the steady-state solution, which reads:

$$u_1 = -\frac{1}{2\mu_1}y^2 + \frac{3\mu_1 + \mu_2}{\mu_1^2 + \mu_1\mu_2}y \quad (5.13)$$

$$u_2 = -\frac{1}{2\mu_2}y^2 + \frac{3\mu_1 + \mu_2}{\mu_2^2 + \mu_1\mu_2}y + \frac{4(\mu_2 - \mu_1)}{\mu_2^2 + \mu_1\mu_2} \quad (5.14)$$

Analysis shows that both of these parabolas share the same location of their maximum, at  $y = (3\mu_1 + \mu_2) / (\mu_1 + \mu_2)$ . As such, the solution will always be of a shape similar to the one in Fig. 5.7.

To verify that the two-fluid Poiseuille model works, the rate of convergence has been analysed. The results are in the following table.

Number of iterations	15000	20000	30000
<b>8 grid points</b>	19.48529607	19.84962771	19.98716522
<b>16 grid points</b>	19.48886924	19.8510184	19.98734291
<b>32 grid points</b>	19.48988285	19.85141221	19.98739307
$2^p$	3.525192135	3.5313729971	3.5424641147
<b>16 grid points</b>	19.48886924	19.8510184	19.98734291
<b>32 grid points</b>	19.48988285	19.85141221	19.98739307
<b>64 grid points</b>	19.49015153	19.85151655	19.98740634
$2^p$	3.772554712	3.7742955722	3.7799547852

The same calculations yield  $2^p \approx 4$  for the one-fluid model. This indicates that the coupling does reduce convergence, but only slightly. By increasing the amount of grid points, the convergence becomes remarkably better.

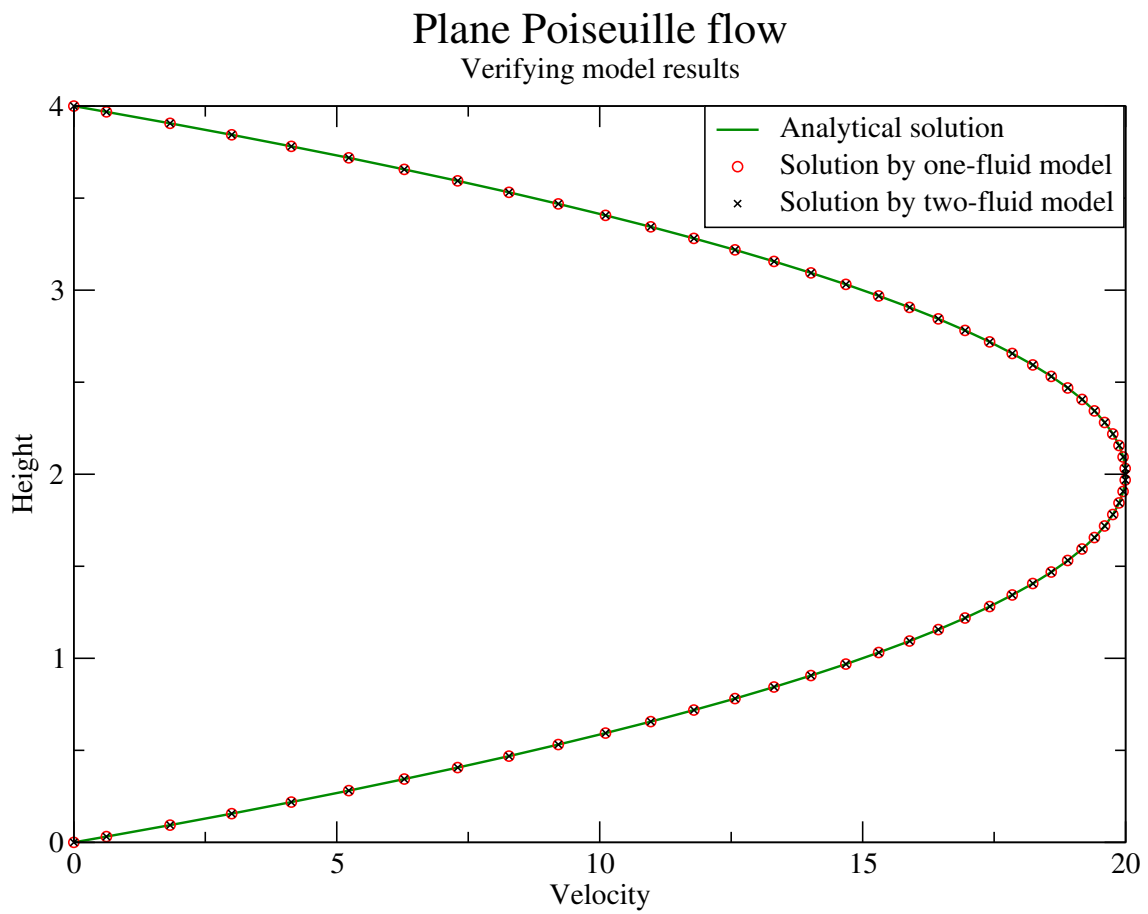


Fig. 5.3: The different models and the analytical solution match

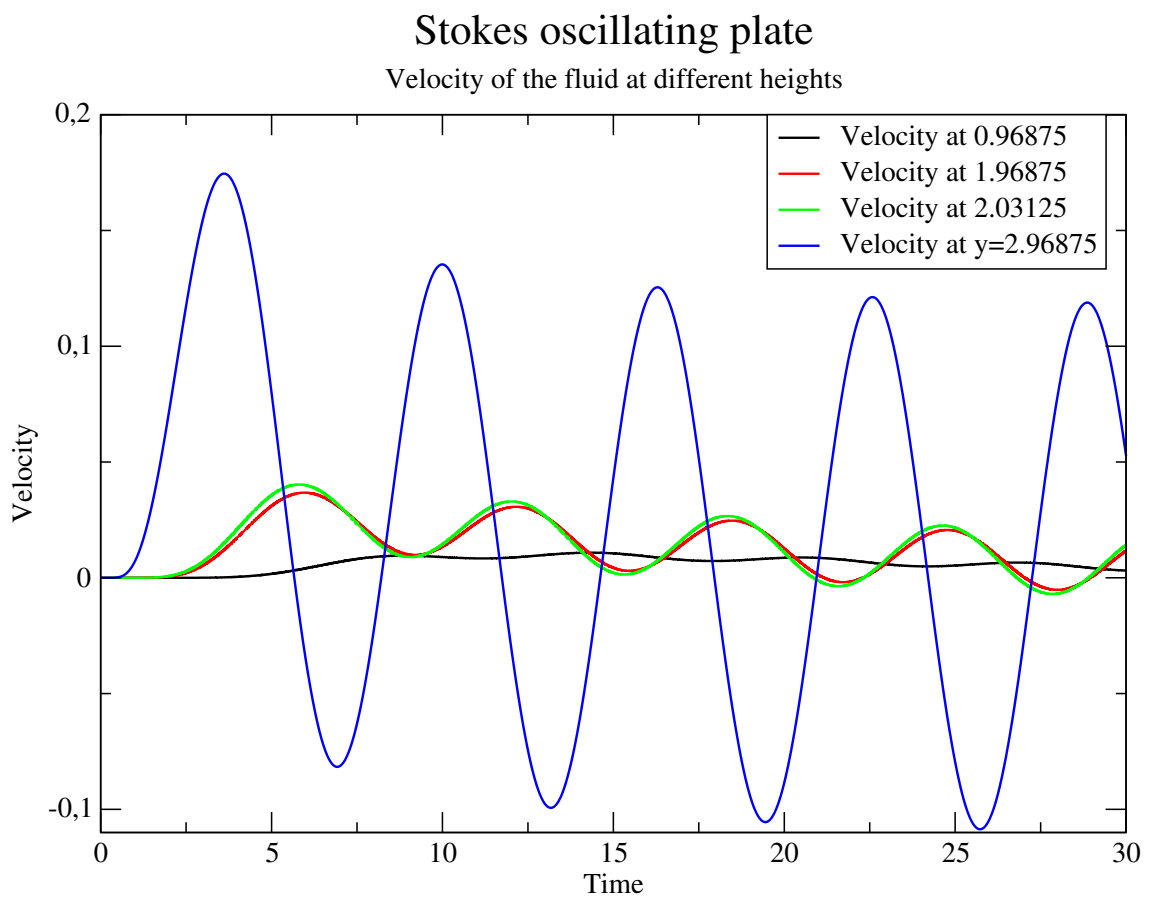


Fig. 5.4: The motion of the fluid in time at different heights

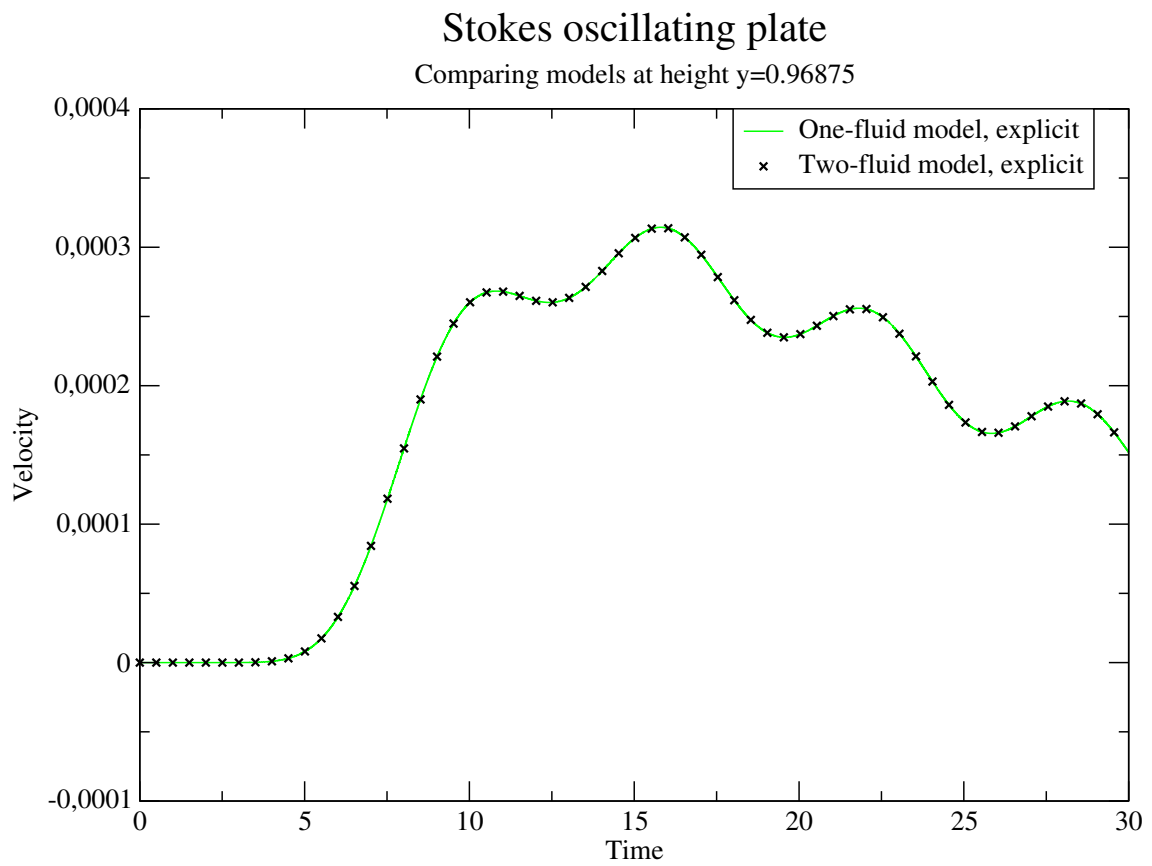


Fig. 5.5: The motion of the fluid at  $y = 0.96875$

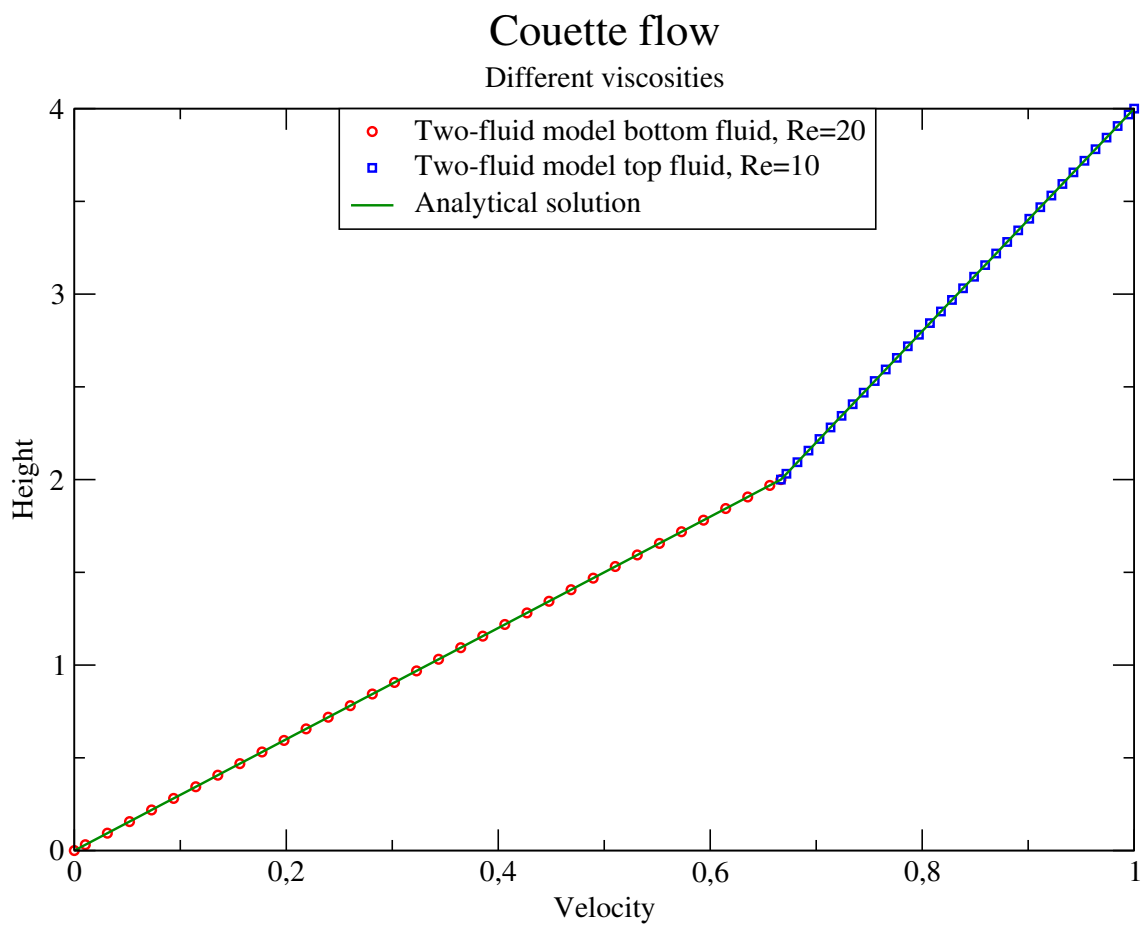


Fig. 5.6: Couette flow with two different fluids

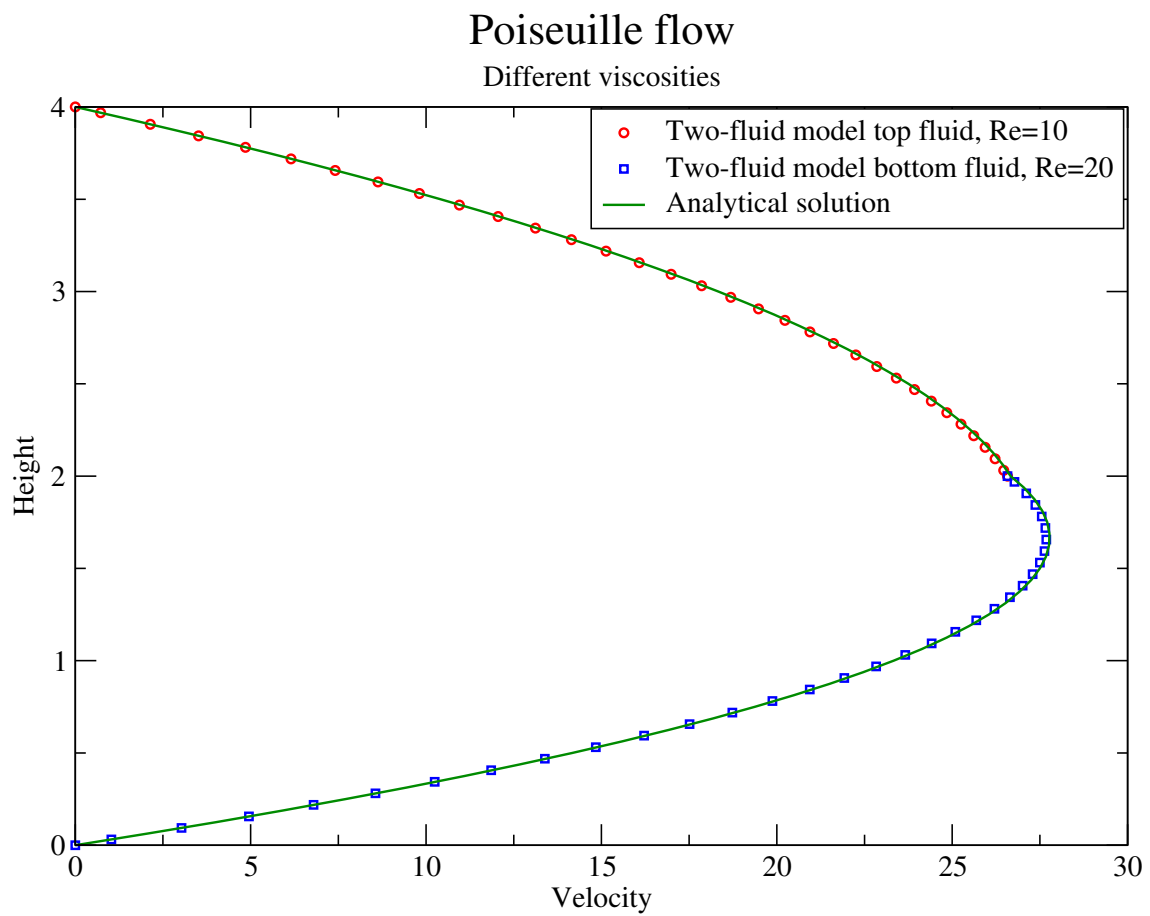


Fig. 5.7: Poiseuille flow with two different fluids



## CHAPTER 6

# BOUNDARY REYNOLDS NUMBER

---

The distinguishing characteristic that separates one fluid from another in the LES-model is the boundary Reynolds number. This is a dimensionless characteristic that generally indicates if a fluid is laminar or turbulent.

Suppose one knows this value for the top fluid,  $Re_{top}$ , then one can calculate the boundary Reynolds number for the bottom fluid. The boundary Reynolds number is defined as:

$$Re = \frac{k_s u_\tau}{\nu} \quad (6.1)$$

With  $u_\tau$  the shear velocity defined as:

$$u_\tau = \sqrt{\frac{\tau}{\rho}} \quad (6.2)$$

And  $\tau$  being the wall shear stress, defined by the density  $\rho$  and the kinematic viscosity  $\nu$ :

$$\tau = \rho \nu \left. \frac{\partial u}{\partial y} \right|_{wall} \quad (6.3)$$

$k_s$  is the characteristic roughness length scale. While the characteristic roughness is not of influence here, the characteristic length differs per fluid. The top fluid starts from a plane poiseuille flow in a closed channel, which has a characteristic length of half the channel. The characteristic length of the bottom fluid is that of an open channel, equal to the channel height.

This yields for the boundary Reynolds numbers:

$$Re_{\tau_{top}} = \frac{h u_{\tau_{top}}}{\nu_{top}} \quad (6.4)$$

$$Re_{\tau_{bottom}} = \frac{2h u_{\tau_{bottom}}}{\nu_{bottom}} \quad (6.5)$$

At the interface there should hold:

$$\begin{aligned} \mu_{top} \left. \frac{\partial u}{\partial y} \right|_{top=0} &= \mu_{bot} \left. \frac{\partial u}{\partial y} \right|_{bot=2} \\ \Leftrightarrow \rho_{top} \nu_{top} \left. \frac{\partial u}{\partial y} \right|_{top=0} &= \rho_{bot} \nu_{bot} \left. \frac{\partial u}{\partial y} \right|_{bot=2} \end{aligned} \quad (6.6)$$

Now, one can fill in (6.3) and (6.6) into (6.2) for the top fluid:

$$\begin{aligned}
 u_{\tau_{top}} &= \sqrt{\frac{\tau_{top}}{\rho_{top}}} \\
 &= \sqrt{\nu_{top} \left. \frac{\partial u}{\partial y} \right|_{top=0}} \\
 &= \sqrt{\frac{\rho_{bottom}}{\rho_{top}}} \sqrt{\nu_{bottom} \left. \frac{\partial u}{\partial y} \right|_{bot=2}} \\
 &= \sqrt{\frac{\rho_{bottom}}{\rho_{top}}} u_{\tau_{bottom}}
 \end{aligned} \tag{6.7}$$

Algebra can then show the relation between the boundary Reynolds number for air and water:

$$\begin{aligned}
 Re_{\tau_{bottom}} &= \frac{2hu_{\tau_{bottom}}}{\nu_{bottom}} \\
 &= \frac{2u_{\tau_{top}}}{\nu_{bottom} \sqrt{\frac{\rho_{bottom}}{\rho_{top}}}} \\
 &= 2 \frac{\nu_{top}}{\nu_{bottom}} \sqrt{\frac{\rho_{top}}{\rho_{bottom}}} Re_{\tau_{top}}
 \end{aligned}$$

The densities and kinematic viscosities are assumed for standard atmospheric pressure at twenty degrees centigrade, for dry air.

$$\begin{aligned}
 \nu_{top} &= 10^{-5} \\
 \rho_{top} &= 1.2041 \\
 \nu_{bottom} &= 10^{-6} \\
 \rho_{bottom} &= 0.998 \cdot 10^3
 \end{aligned}$$

Resulting in:

$$Re_{\tau_{water}} \approx 0.6975 \cdot Re_{\tau_{air}} \tag{6.8}$$

In this case, the Reynolds number in the top fluid is chosen as 180. Then  $Re_{water}$  is 125.0.

## CHAPTER 7

# THREE-DIMENSIONAL SETUP

---

The most interesting case available is simulating the behaviour of two fluids under a three-dimensional flow. For this, a turbulent flow is taken as the top fluid. The type of turbulent flow in this case is the plane channel flow, driven by a pressure gradient in one direction, but clearly turbulent. The case has been well-documented as a test case for a long time, with good documentation in [6].

The setup of this thesis is different, as a turbulent plane channel flow has been taken as the initial condition for the top fluid, while the bottom fluid only has the input through the interface as excitation. No pressure gradient or other force is applied.

A schematic sideview with the imposed conditions can be found in Fig. 7.1. The boundaries in the  $z$ -direction are periodic as well.

The top fluid has a Reynolds number of 180, enough to guarantee a fully turbulent flow. The bottom fluid has a Reynolds number of 125, making the fluids mathematically similar (see Section 6) to the relation between air and water.

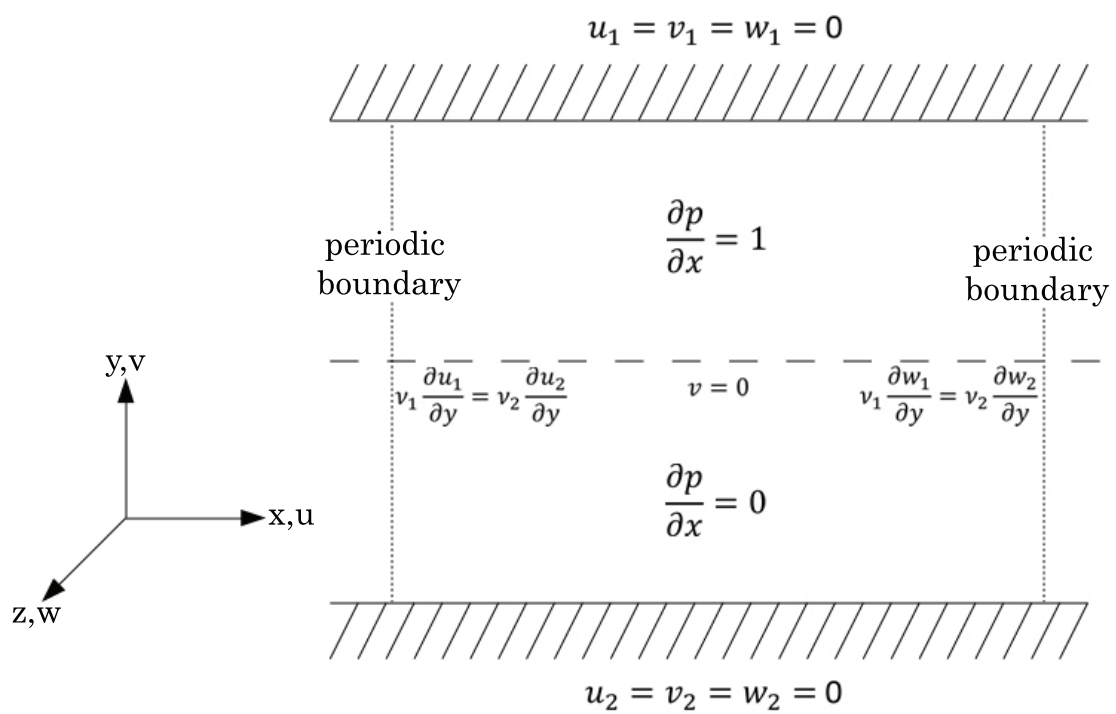


Fig. 7.1: Schematic sideview

# CHAPTER 8

## RESULTS

---

The LES model has been adapted to handle two fluids and has been coupled at the interface. This verified model has then been set to simulate a fluid flow with Reynolds numbers of 180 and 125 for the top and bottom fluid respectively. The initial condition is a turbulent flow for the top fluid and a motionless fluid for the bottom. The Courant number is kept constant to ensure stability for the semi-implicit scheme.

To be able to create results, it is required that the flow reaches a steady state. This can be discerned in multiple ways, the easiest of which are by analysing the wall shear stresses and by analysing the total shear stress in the entire domain. The first method is from an equilibrium consideration; the combined wall shear stress present in the gas system (where the pressure gradient is applied) should be equal to two, to balance the pressure gradient. Mathematically,  $2h\Pi = \tau_{int} + \tau_{wall}$ . The pressure gradient is of size one, applied over a height of two. The shear stress at the interface plus the shear stress at the wall added together are 1.987. The small discrepancy is caused by variance and possibly imperfect measurement of the gradient at the wall, using a forward derivative. Later, further confirmation of the steady state will be given by looking at the shear stress present in the entire channel.

Just as important as the steady-state, is the fact that a turbulent flow is not random at all times. To be able to apply statistical methods to analyse the results, it is required that the snapshots of the turbulent flow are independent identically distributed events. The autocorrelation has been calculated at three points, namely the viscous sublayer of the top fluid, the inner region of the turbulent flow and the transitional region of the bottom fluid. From Fig. 8.1 it is clear that flow fields can be considered independent if there is a temporal distance between them of at least 0.5. It is also visible that in the viscous layer, the flow field is much slower to change than in the inner regions. Also, despite the fact the flow did not contain turbulence at first, the bottom flow is still very much influenced by turbulence in the steady state.

The other tool that correlation gives is the spatial correlation. A high spatial correlation will indicate that the flow is very similar, while a spatial correlation close to zero indicates that there is barely any similarity. For this analysis, four measuring points have been taken, at  $y^+ = -127.6, 1.058, 10.88, 149.7$  in the gas. In Fig. 8.2, the correlation of the streamwise velocity has been taken from these points. In this graph, the measuring is done in the direction of the liquid. That means that for the point  $y^+ = 1.058$ , which is the first grid point above the interface, the first correlation will be with  $y^+ = 0$ . It quickly becomes clear that what happens near the interface is the most highly correlated with the flow in the liquid, never becoming entirely uncorrelated. For the measuring point  $y^+ = 10.88$ , the effect is even more drastic, with almost no correlation left below the viscous boundary layer on the bottom side of the interface,

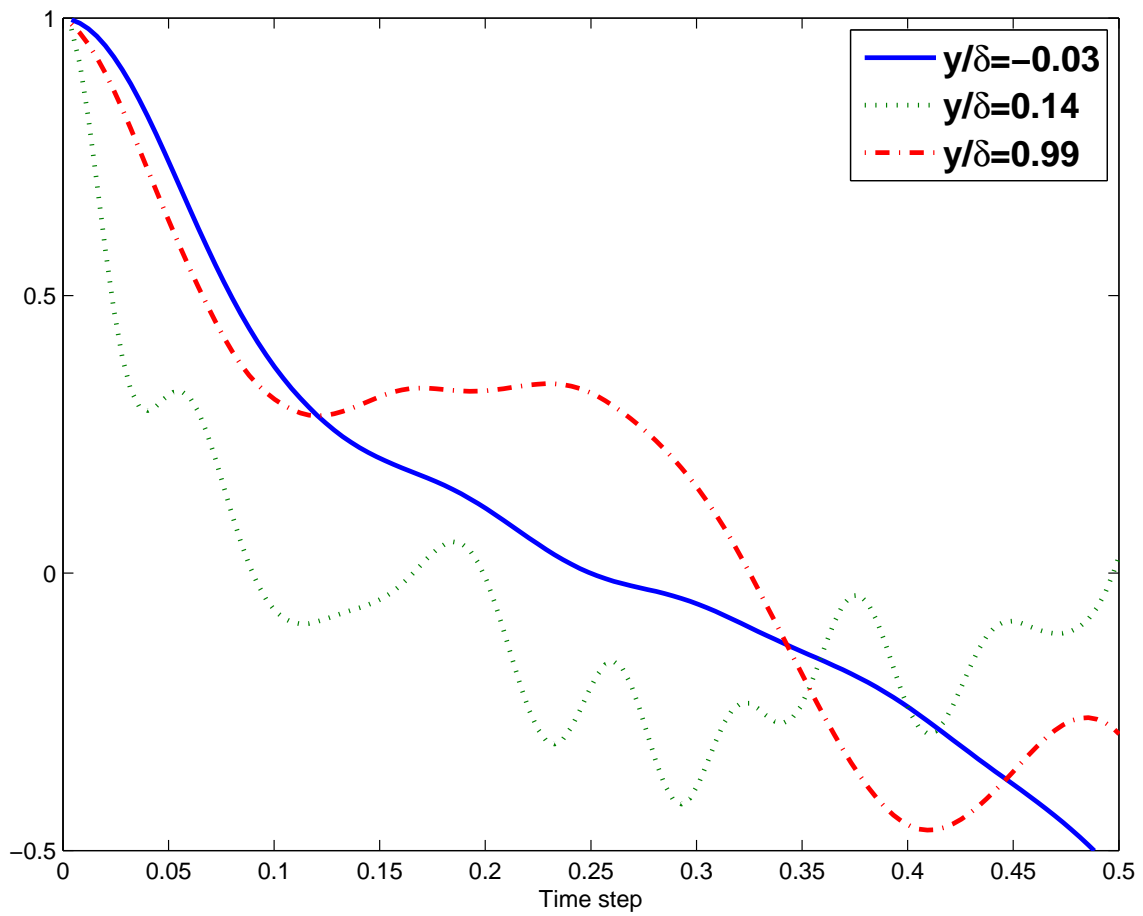


Fig. 8.1: The autocorrelation for a turbulent flow

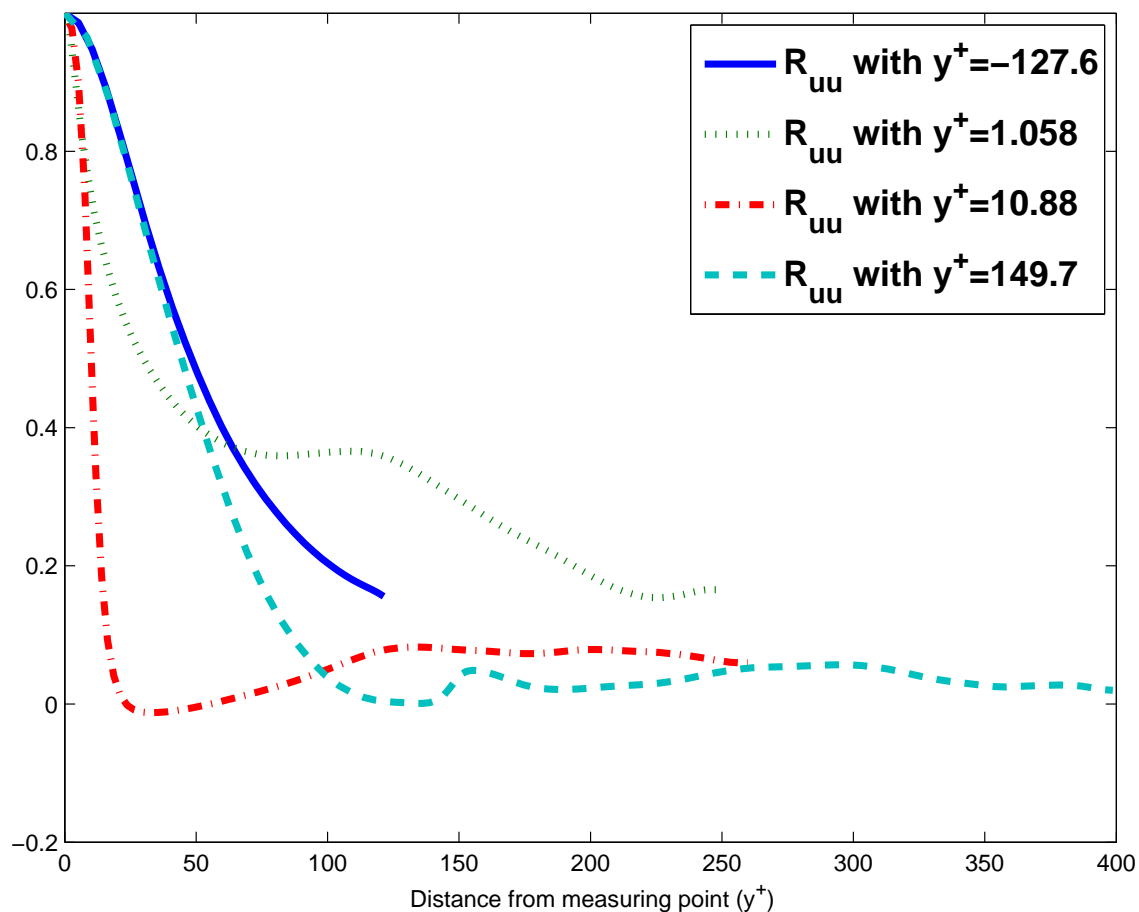


Fig. 8.2: The spatial correlation for a turbulent flow, measuring towards the bottom of the domain

but the decrease in correlation drops considerably. It is clear that most of the flow in the liquid is highly correlated, as seen by the behaviour of the line  $y^+ = -127.6$ .

Looking at the correlation to the other side in Fig. 8.3, it becomes apparent that this process goes much more smoothly for the measuring points inside the gas, as one would expect in a single fluid flow. Only the top measuring point,  $y^+ = 149.7$ , doesn't have enough spatial room to reach zero correlation. However, the line  $y^+ = -127.6$  shows a sharp correlation drop immediately after crossing the interface. From this, it is seen that what happens on the gas side influences what happens on the liquid side much more than the other way around.

This lays the basis to get a grip on the flow behaviour. To start, the mean velocity profile can be found in Fig. 8.4. The profile in the lower fluid (below the height of two) shows a clear Couette flow: linearly decreasing the velocity in the inner region, while viscous effects dominate in the boundary layers. The top layer would be a Poiseuille (plane channel) flow with a maximum velocity in the middle, if the interface was a wall. Now it is seen that instead of a symmetric parabolic profile, the maximum velocity is located closer to the interface. Note that this profile and all others where it is applicable, have been normalised (NOTE: the axes will still

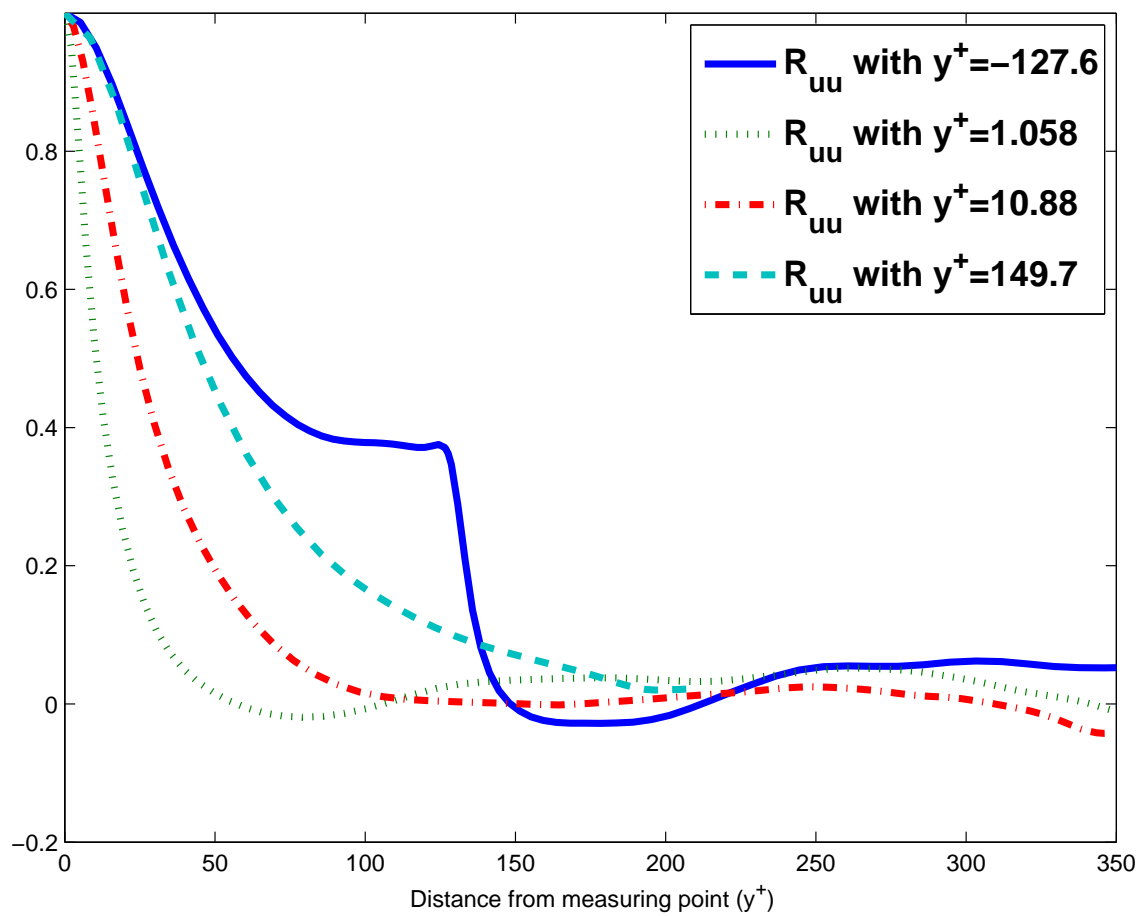


Fig. 8.3: The spatial correlation for a turbulent flow, measuring towards the top of the domain

have to be normalised in some cases).

The next interesting characteristic of the flow is the root mean square (rms) of the velocities, in Fig. 8.5. Near the top wall, the behaviour of the flow is very similar to that of the behaviour seen in plane channel flow (Fig. 6 of [6]). The difference becomes visible from the middle of the channel. Here, the rms steadily decreases towards the interface and only starts to increase again at the point where the mean velocity starts to decrease (see Fig. 8.4). Close to the interface, the rms velocities decrease noticeably. This can be expected, as the coupling has been done viscously and forces from one fluid as such do not easily transfer to the other fluid. Therefore, the fluctuations will also be less.

In the liquid, the normal and spanwise rms-velocities are symmetric, as expected in a Couette flow. However, the streamwise rms-velocity is slightly asymmetric, with a lower rms near the interface. The asymmetry is a direct result of the presence of this interface instead of a wall. Thus this type of interface decreases the nearby turbulence in a flow. This is in good agreement with the result of [3], where the same conclusion was reached for a deformable interface.

Comparing these results to those of [8], there is an increase of rms on the liquid side. However, for smaller differences between their Reynolds number, this effect is not observed, leaving the conclusion that the nondimensional rms of the liquid side is higher than that of the water side, which is also observed here.

A further analysis includes the Reynolds shear stress,  $u'v'$  and the total shear stress, comprised of the Reynolds shear stress and the extra term  $(1/Re) \partial \bar{u} / \partial y$ . These are found in Fig. 8.6. The straight line in the gas of the total stress, which is associated with a pressure-driven channel flow, indicates that a steady state has been reached. Furthermore, the straight line of the stresses in the liquid also indicate the stresses associated with a steady state Couette flow. Also, the boundary condition of continuity of shear stress is clearly visible.

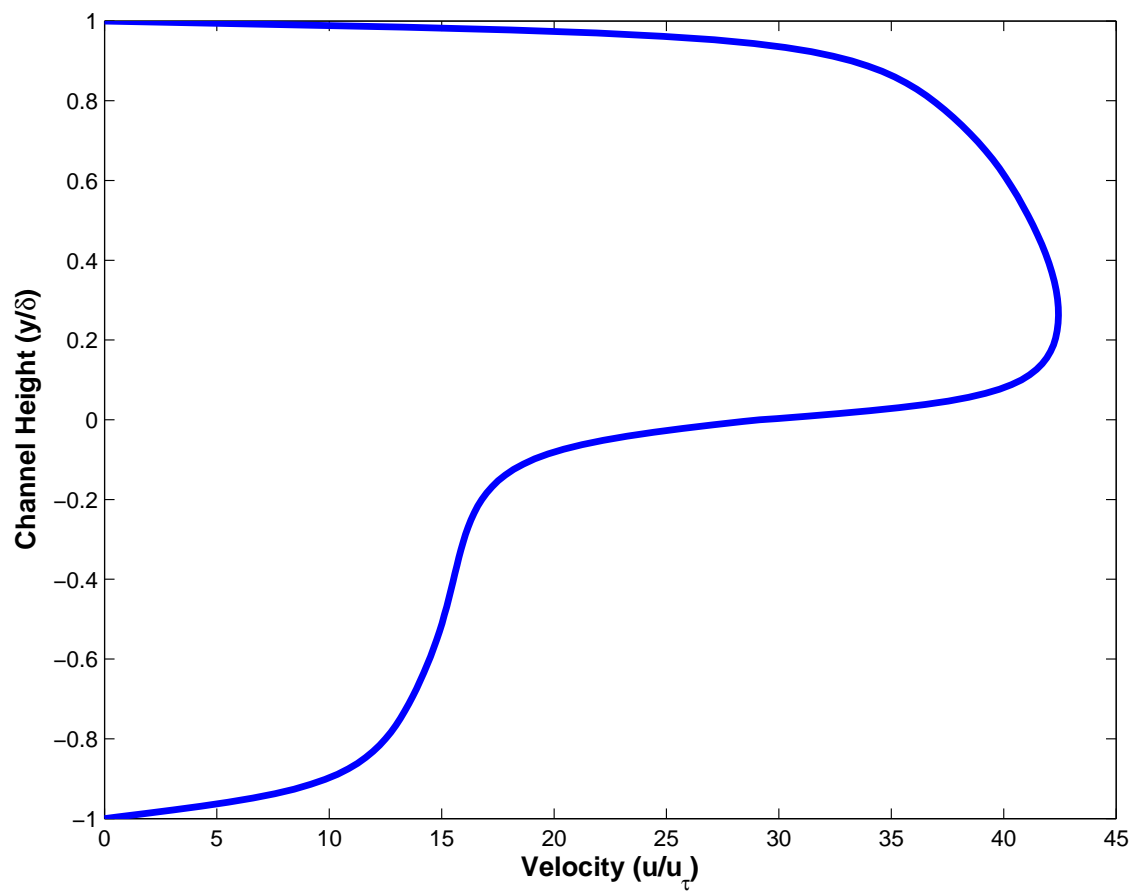


Fig. 8.4: The mean velocity profile of the turbulent flow

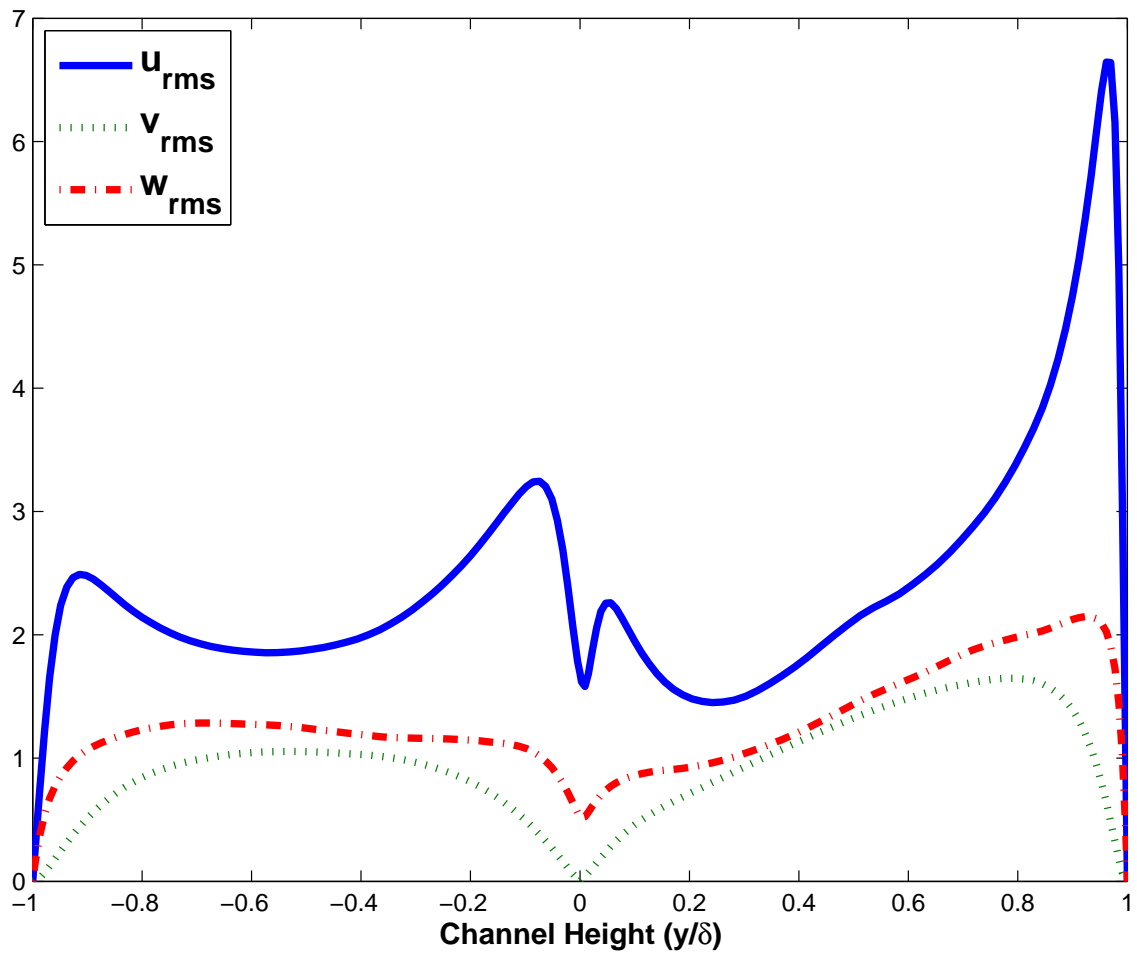


Fig. 8.5: The root mean square velocities of the turbulent flow

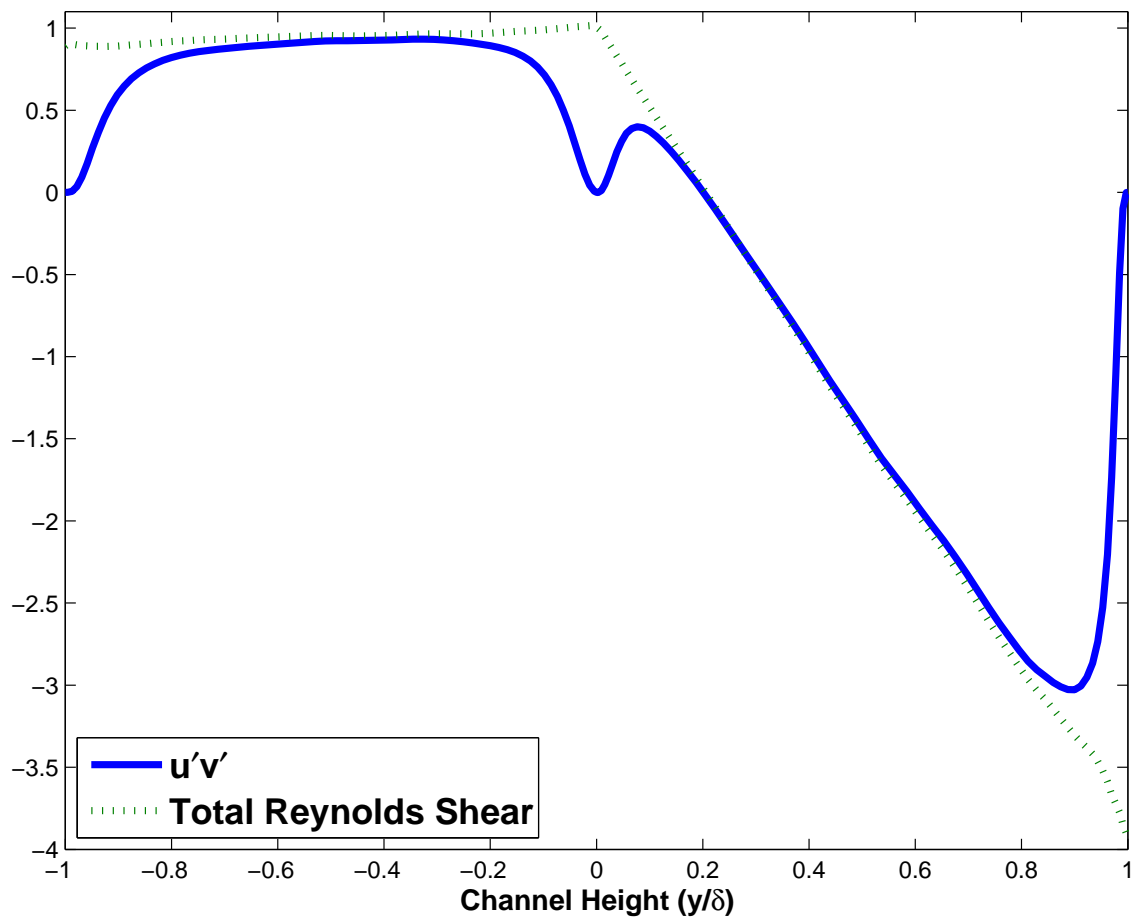


Fig. 8.6: The shear stresses of the turbulent flow

## 8.1 Quadrant Analysis

In [8], the most interesting conclusions were obtained by looking at the behaviour of different types of turbulence near the interface using quadrant analysis. A clear distinction could be made between the behaviour on the gas side, the shear stress at the interface and the behaviour on the liquid side. This was in a very comparable flow, with the only difference in the setup of the simulation being a pressure gradient opposite to the pressure gradient in the gas. In that article, the fluids were also comparatively like air and water. They found that on the gas side, so-called sweeps dominate over high-shear regions and ejections dominate over low-shear regions, while on the liquid side, there was no such relation.

Four types of turbulent events, called quadrants, are generally identified. The orientation of these events is in the streamwise direction and away from the interface. They are classified by the sign of  $u'$  and  $v'$ , the deviation of the average of the streamwise and normal velocities. For the gas, the definition is as follows. For the liquid, the vertical orientation is the other way around. The first quadrant, when  $u' > 0$  and  $v' > 0$ , is high-speed fluid motion, directed away from the interface. The second quadrant is when  $u' < 0$  and  $v' > 0$ . These are called ejections and contain low-speed fluid moving away from the interface. The third quadrant,  $u' < 0$  and  $v' < 0$ , is comprised of low-speed fluid moving to the interface. Finally, the fourth quadrant events,  $u' > 0$  and  $v' < 0$ , are called sweeps and contain high-speed fluids directed towards the interface.

A coherent event in the boundary layer is defined similarly to [8]. Measurements have been done at five points below a distance  $y^+ = 12$  on both sides of the interface, inside the viscous boundary layer. If at four of these five points, the same quadrant was present, it has been defined to be a coherent event. The points above the interface are  $y^+ = 1.06, 3.26, 5.62, 8.16, 10.88$ . Below the interface the points are different, due to different grids based on the viscosities,  $y^+ = 1.04, 3.18, 5.43, 7.79, 10.27$ . The difference in location is not expected to make a significant difference, because the measurement locations are still very similar and the coherence of events will be registered over the same non-dimensional boundary layer. In [8] the results showed clear relations between the shear stress at the interface and the presence of different types of events, as well as a distinction between the type of events inside the boundary layer and outside.

A first indication of the behaviour of the turbulence is made by looking at the fractional contribution of each quadrant to the total presence at each  $x, z$ -plane away from the interface (Figs. 8.7 and 8.8). Because of the orientation, the first and third quadrant events are positive in the gas, while they are negative in the liquid.

In Fig. 8.8, it is seen that sweeps are more common everywhere near the interface, with the ejections only becoming dominant far away from the interface. In [8], they found that this switch occurred much more near the interface. It seems that a pressure gradient has an effect on the behaviour of ejections and sweeps.

On the other hand, the gas does contain a pressure gradient and Fig. 8.7 is very similar near the interface to the ones in [8]. The real difference is in the strength of the turbulence in

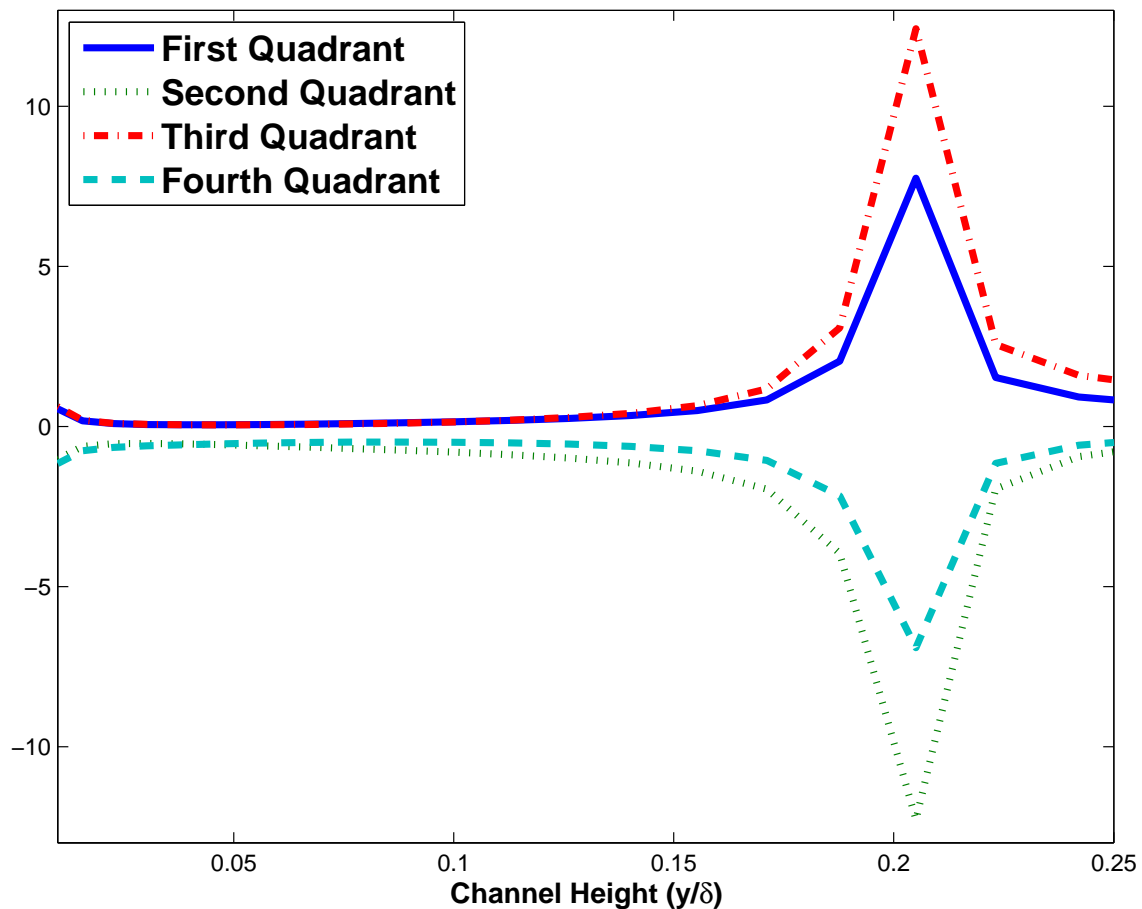


Fig. 8.7: The fractional contribution of quadrants in the gas

the region  $0.15 < y/\delta < 0.25$ , where the intensity of all events takes on huge proportions. This is just below where the maximum velocity is found, showing there is increased turbulence in specifically this area of a channel flow like this. The switch between prominence from ejections near the interface to sweeps away from the interface happens around  $y/\delta = 0.05$ . For the prominence of first quadrant events, this happens in the region  $y/\delta = 0.03$  to  $y/\delta = 0.11$ . However, their behaviour is almost indistinguishable near the interface. This can be seen in Fig. 8.9.

The conclusion is that the pressure gradient influences the behaviour of ejections and sweeps near the interface, as well as that the turbulence intensity in the gas flow in the region  $0.15 < y/\delta < 0.25$  is very large.

To find a relation between events and shear stress, the probability of an event occurring dependent on the observed interfacial shear stress has been made visible in Figs. 8.10 and 8.11, for the gas and liquid respectively.

For the gas, the quadrants with their probabilities look very similar to those found in Fig. 22a of [8], with the second and fourth quadrants having the highest probabilities of occurring, in addition to ejections tending to occur over regions with low stress and sweeps over regions of

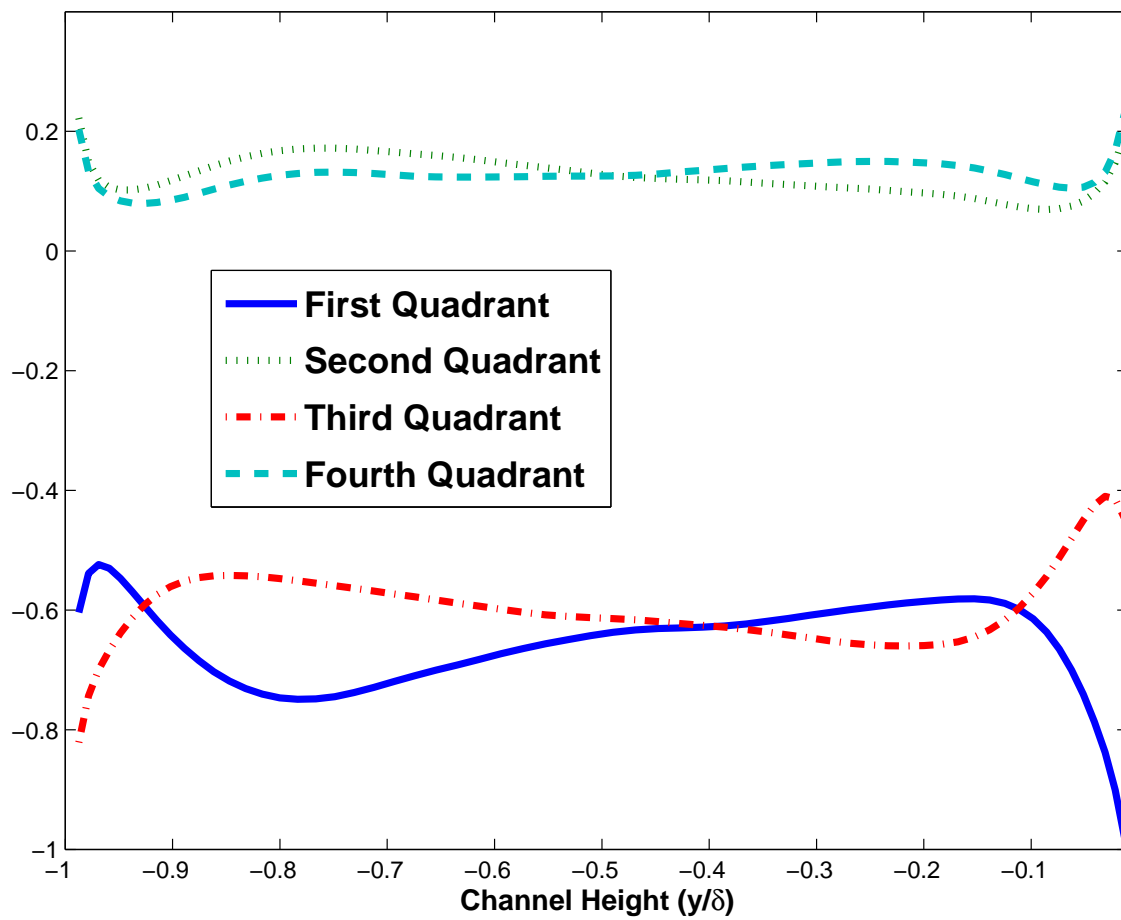


Fig. 8.8: The fractional contribution of quadrants in the liquid

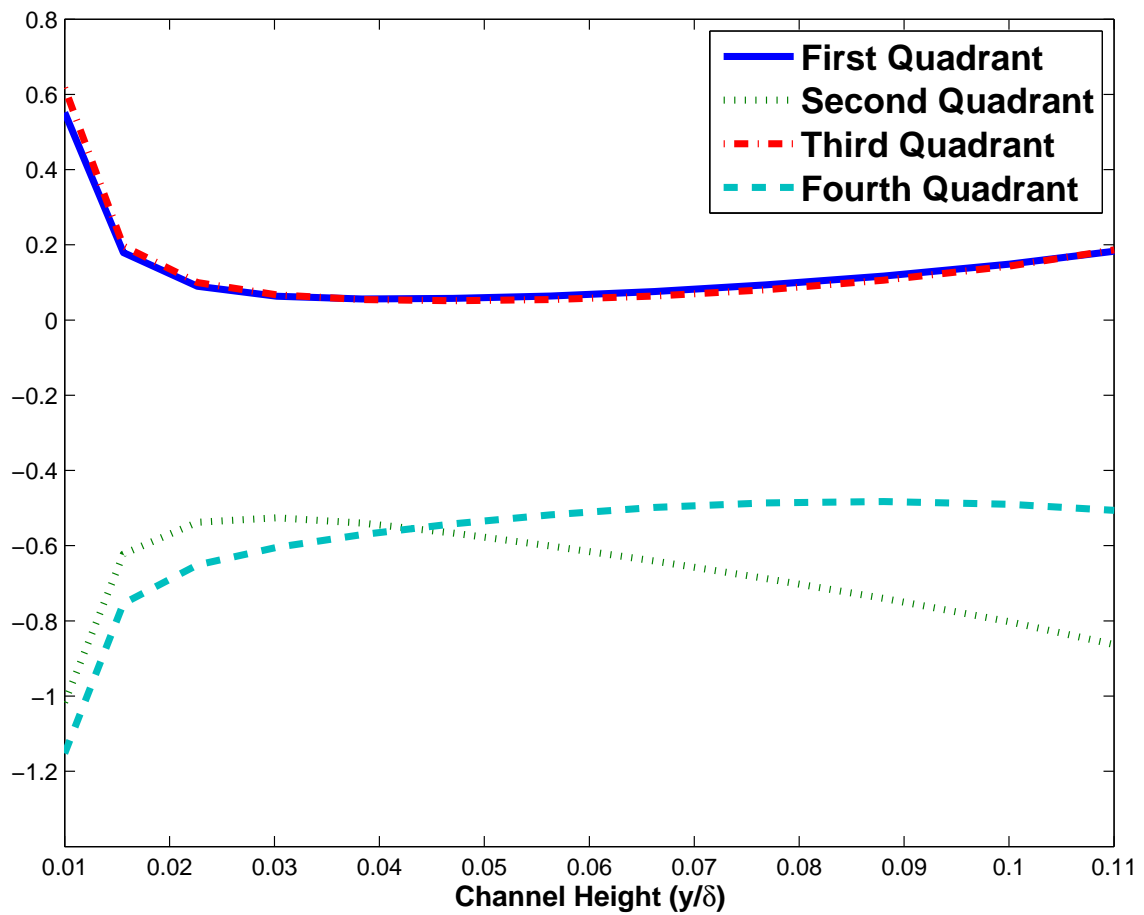


Fig. 8.9: The fractional contribution of quadrants in the gas, zoomed in

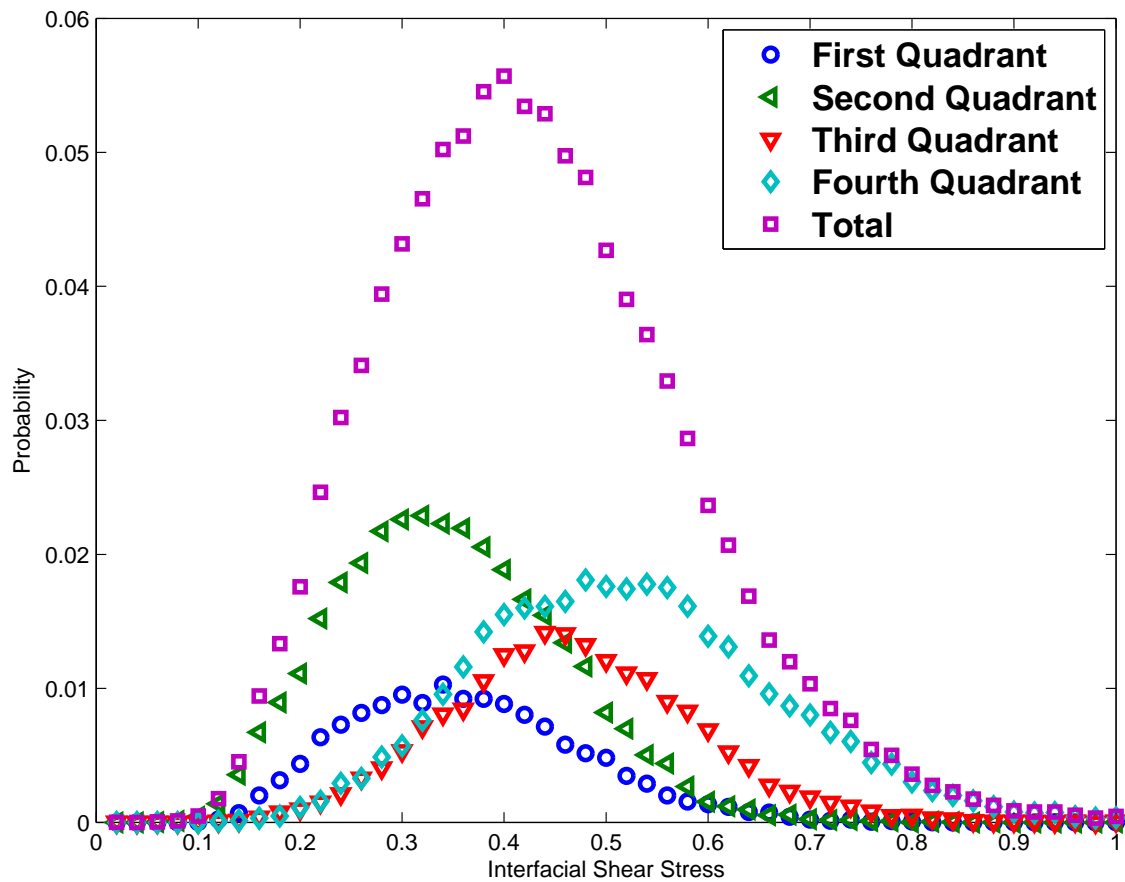


Fig. 8.10: Probability functions based on the interfacial shear stress, gas side

high stress. The explanation that a high speed to the interface will also contribute the most to the high stress regions, holds. In the liquid, however, the phenomenon is different. In Fig. 8.11 it is seen that events of the first and third quadrant, instead of the second and fourth quadrant, contribute the most to the events and exhibit the observable shear-stress dependence. This means that in the liquid, outward motion of high-speed fluid is largely associated with low shear, while inward motion of low-speed fluid is associated with high shear stress.

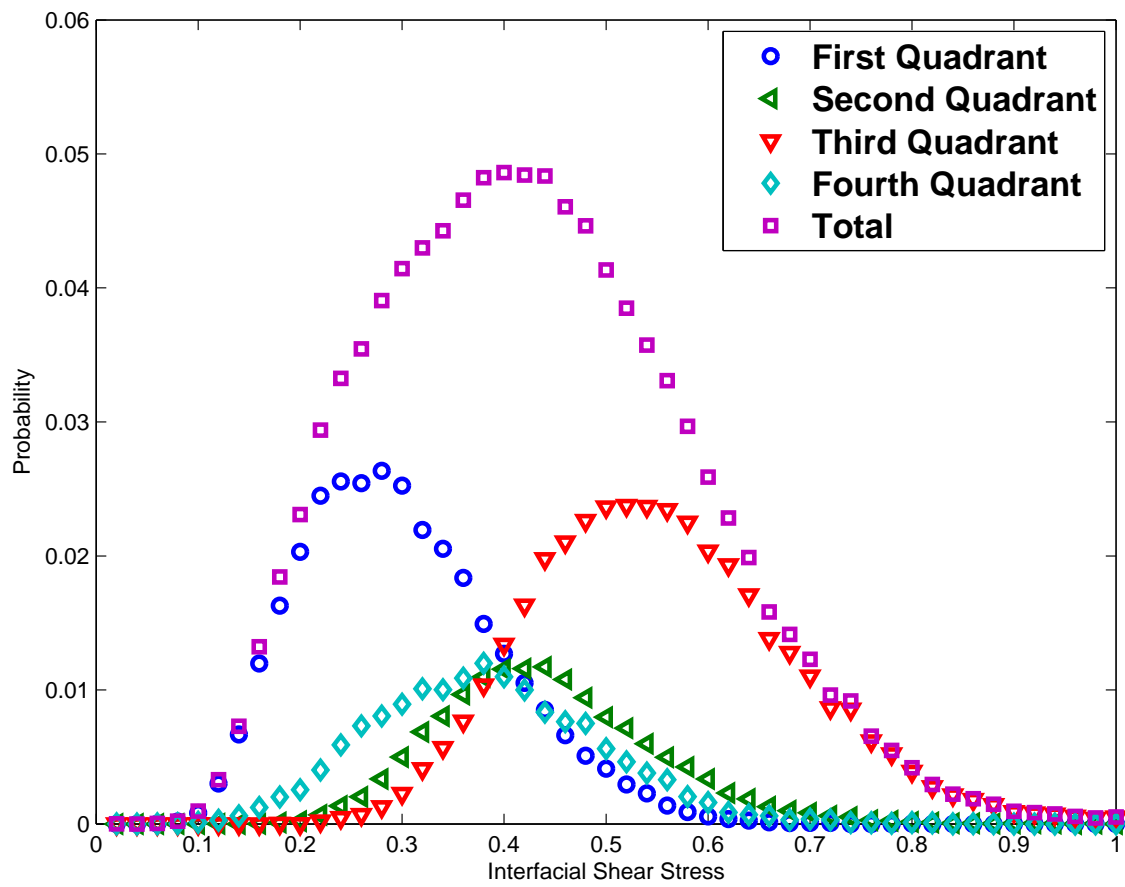


Fig. 8.11: Probability functions based on the interfacial shear stress, liquid side

The next step in analysing this behaviour in the interface is to find the correlation between simultaneous events on both sides of the interface. The only events considered here are those when there is an event above the interface as well as one below the interface, so-called coupled events, . The contribution of the combination of these events to and against the total shear stress has been displayed as a cumulative distribution function in Fig. 8.12. This graph contains the eight biggest contributors, which amount to 95% of the total shear stress. The other eight combinations are significantly less, as can be seen in Fig. 8.13. The events are named by two numbers, the first number being the event taking place in the gas and then the second number the corresponding event in the liquid.

Of the eight biggest contributors, four of them are the same events coupled. Because the interface is flat and transmits no information regarding vertical fluctuations, it is expected that events with the same sign for  $u'$  happen simultaneously. In addition to this, similar events occur over the same kind of region. As such, it is far more likely, for example, that a sweep occurs over a high shear region, where on the other side there is also a sweep corresponding to a high shear region, than it is likely that a sweep occurs on one side and an ejection, associated with low shear, occurs simultaneously.

The reasoning of events occurring over the same kind of region also explains the other two large contributors. Over high stress regions, there is a good chance of a fourth quadrant event above the interface and also of a third quadrant event below the interface, so their coupled appearance is no surprise (4-3). The other is a second quadrant event above the interface with a first quadrant event below the interface (2-1), which occurs over low-stress regions.

This explains six of the eight, but leaves two frequent combinations unexplained (2-3 and 4-1), both of which concern events with a tendency to a different kind of stress region. More scrutiny is required in how events are recognized and measured.

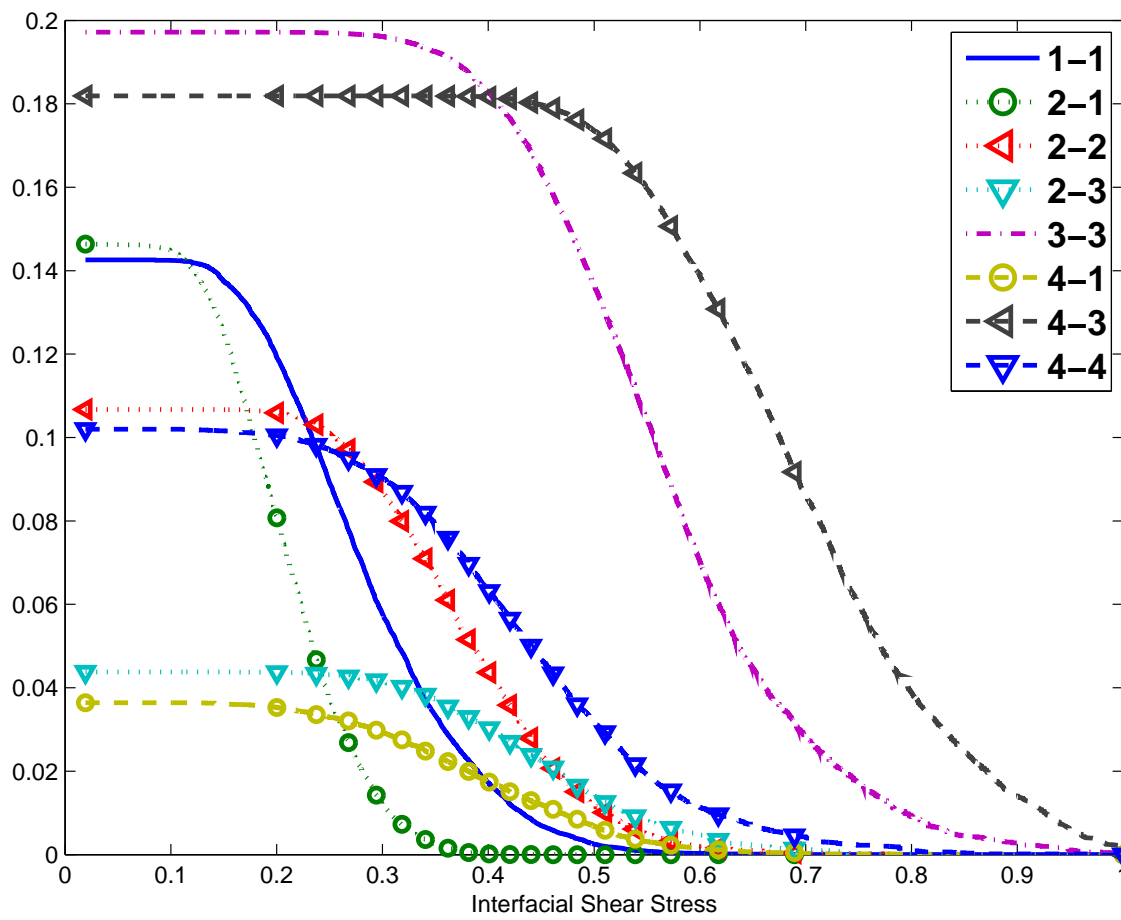


Fig. 8.12: Cumulative distributive function of the coupled events with the highest relative contribution

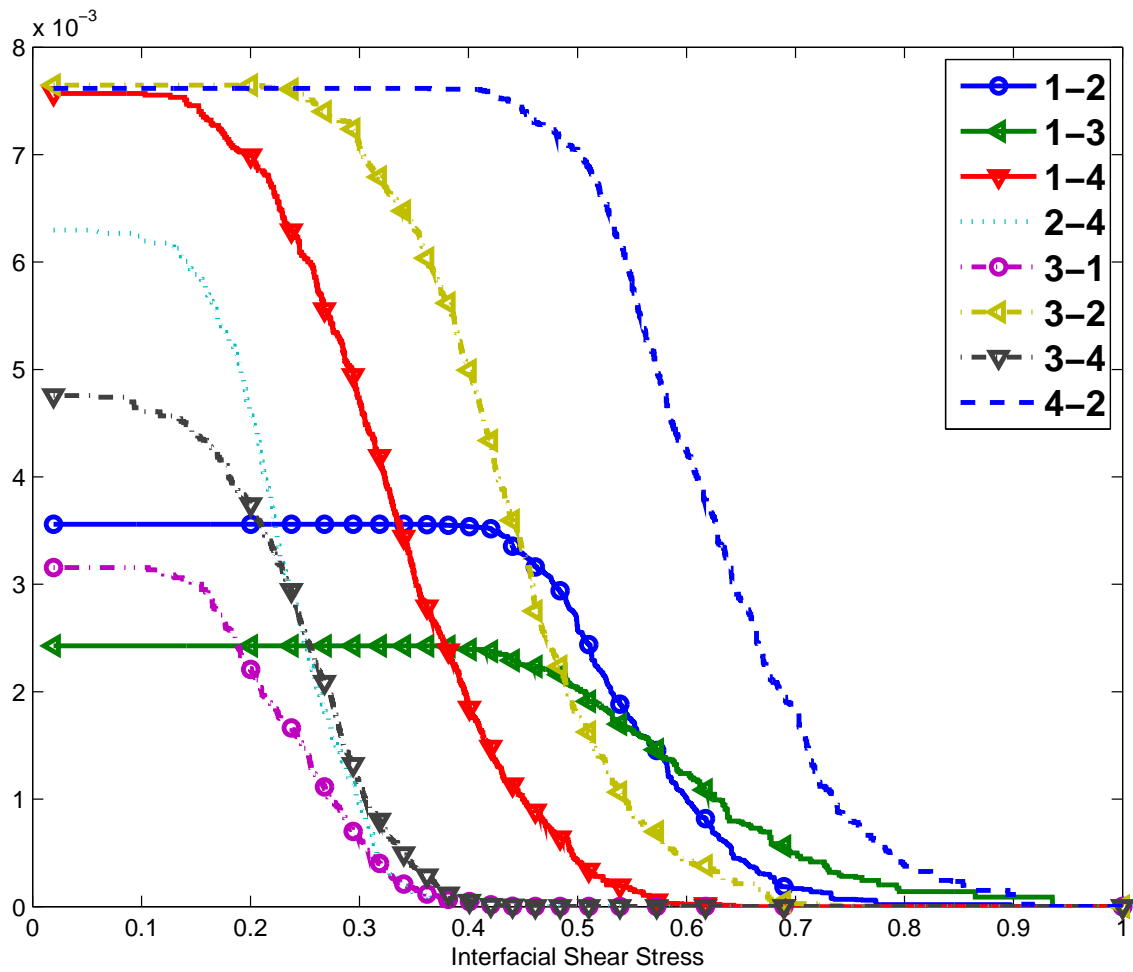


Fig. 8.13: Cumulative distributive function of the coupled events with the lowest relative contribution

The currently used method has two clear disadvantages: all events are considered, but there are a lot of room for false positives. The only requirement for an event is based on the sign and the coherence. The odds are significant (6.25%) that four out of five points are randomly the same event, when there is no event happening. Furthermore, events occupy a space, but the current analysis only analyses whether events happen in one grid cell. The spatial presence of an event is uncertain.

To analyse this spatial presence, the different quadrants have been visualised (in colour only) near the interface. In Fig. 8.14, light blue is quadrant one, green is quadrant two, yellow is quadrant three and red is quadrant four. The vectors indicate the location of the calculated velocities, as well their streamwise and normal direction. Dark blue is the interface and everything outside the viscous layer, artificially put to zero. The green present between the interface and the first grid point is because the drawing program expects a continuous flow field and infers that the velocity must be average between the grid points, while it's actually visualising quadrants instead of velocity.

In Fig. 8.14 it becomes clear that these events also have a spatial presence, with this snapshot showing events of three types clearly having a spatial presence. Other figures would only reinforce this strong spatial presence of events, it has been observed everywhere.

To amend the second possible issue, a split has been made to remove the events with very little contribution, those who actually deviate very little from the average. The threshold has been put at  $\sum u'v' > 1.75 \overline{\sum u'v'}$ . This removed roughly forty percent of the coupled events, leaving only the strongly coupled events.

In Fig. 8.15 the eight biggest contributors are displayed when this threshold is used. These eight now comprise of over 96 percent of the total shear stress contribution by strongly coupled events. The highest contributor of the other eight is at 1.1 percent.

The results are not notably different, so the appearance of specifically these eight combinations is no coincidence. Now, instead of reasoning from earlier graphs to explain this one, it is more interesting to look at what this graph actually tells about turbulent behaviour near the interface.

Looking at the combination 3-3, it becomes apparent that all other combinations with a type 3 turbulent event in the air rarely occur, if ever. Therefore, if there is an event of type 3 near the interface and it is coupled (which is about sixty percent of the time, of which sixty percent again is strongly coupled), it will be with the same type of event. That it is an event with a similar streamwise speed is to be expected due to the coupling, but the fact that the event on the other side is also oriented towards the interface is surprising. The lack of communication with regards to the normal velocity between either side of the interface would lead one to expect that 3-3 events are as common as 3-2 events, but the turbulence clearly exhibits other behaviour.

Taking a look at other events, it becomes clear that all combinations between similar events show this behaviour, with 1-1 also being the only combination present for type 1 turbulent events at the gas interface. On the other hand, on the liquid side of the interface, 2-2 and 4-4 events are the only ones with a significant appearance for ejections and sweeps respectively.

The other four big contributors to coupled events, are the combinations between ejections

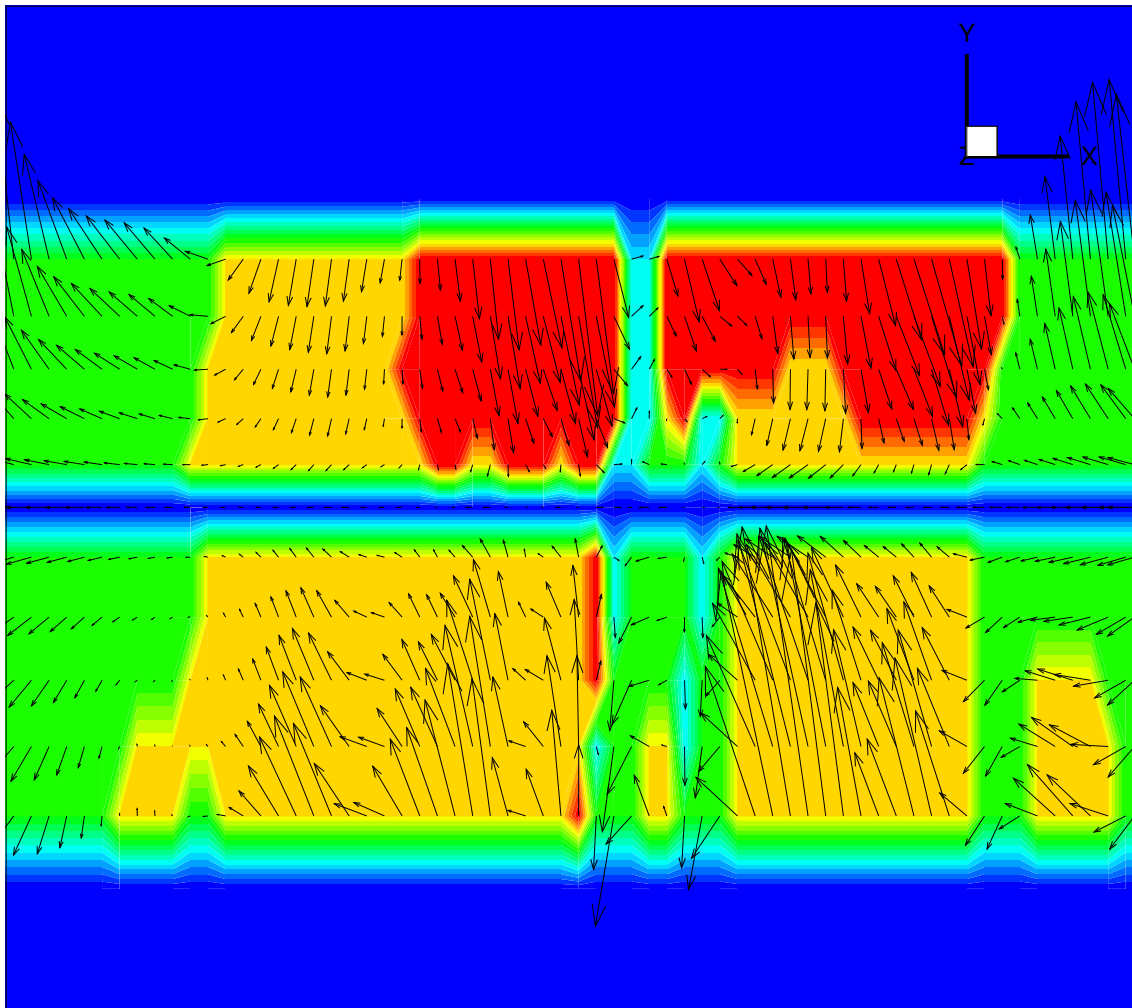


Fig. 8.14: Quadrants near the interface

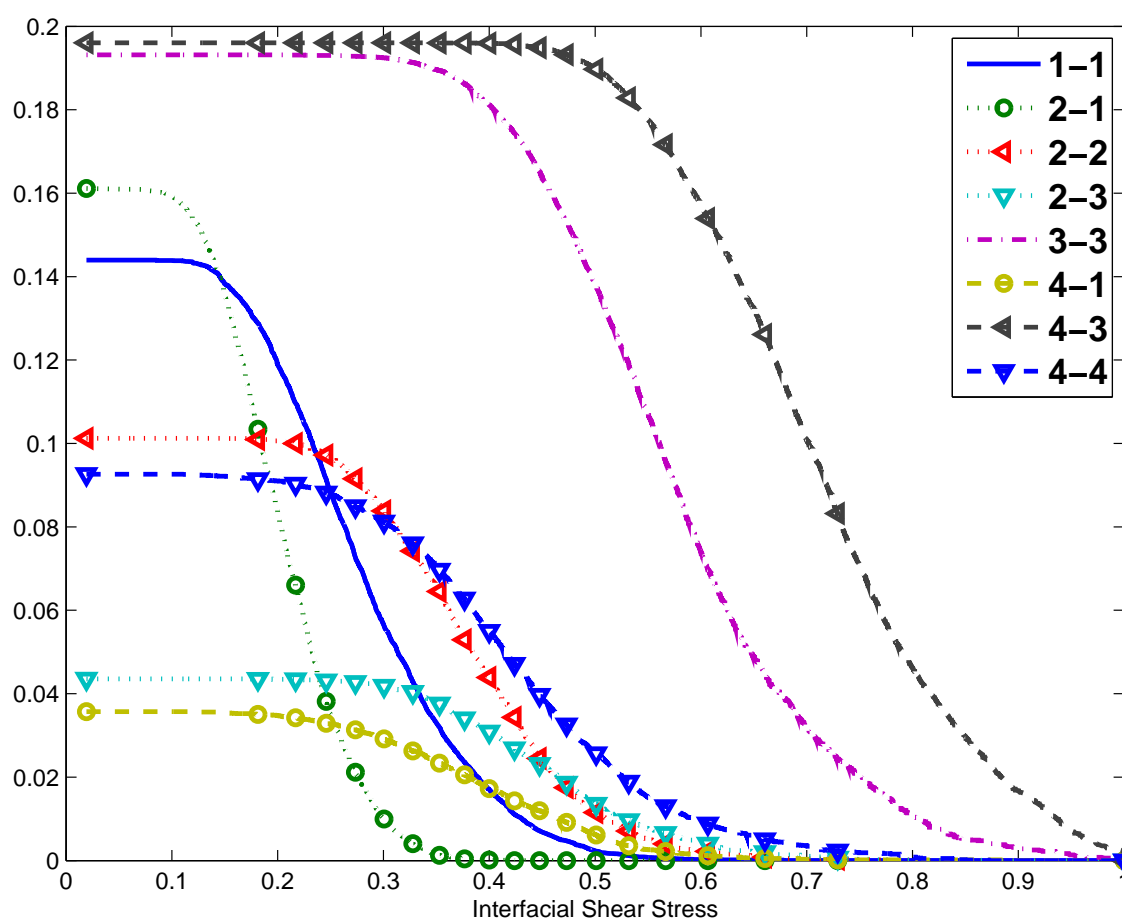


Fig. 8.15: Cumulative distributive function of the strongly coupled events with the highest relative contribution

and sweeps on the gas side and first and third type turbulent events on the liquid side. These are the events with the highest probability of occurring on both sides respectively (see Figs. 8.10 and 8.11). Where there was a significant difference in the probabilities of occurrence of events on a side of the interface, the disparities were not so large as to make one suspect that the differences in coupled events would be so big. Looking more specifically at these four combinations 2-1, 2-3, 4-1 and 4-3, it becomes clear that there is again a disparity in the shear regions. The combination 4-3 happens over high shear regions, as both events happen over high shear regions with large frequency, but 4-1 is a combination between high and low shear tendencies, leading to events occurring from  $\tau_y = 0.2$  to  $\tau_y = 0.6$ . What this means is that a sweep on the gas side will be coupled with a first quadrant event if it occurs over average stress regions, while it will be coupled with a fourth quadrant event over high stress regions. Conversely, ejections on the gas side will be coupled with a first quadrant event over low stress regions, while it will be coupled with a third quadrant event over average stress regions.

Finally, the conclusions of [8] were that on the gas side, sweeps dominate over high shear regions and ejections over low shear regions. The same can be seen here. They also found

that on the liquid side, no such relation was visible. In this simulation, it is shown that there is a strong relation between first quadrant and third quadrant events, for low and high shear stress events respectively, on the liquid side. The difference between these two simulations is that Lombardi et al., [8], had also imposed a pressure gradient on the liquid, which in the gas has shown to increase the number and strength of sweeps and ejections. It is likely that the same effect was present in the liquid then, obscuring the tendency for the more viscous liquid to exhibit first and third quadrant events in reaction to the turbulence in the gas.

Furthermore, between coupled events it becomes clear that the two least common types of events on a side are almost always coupled with the same type of event on the other side, if they are coupled. The turbulence in the streamwise and spanwise directions has a direct influence on the complete turbulent behaviour on either side and in that way also exerts influence on the orientation of events on either side of the interface. In addition, it is seen that the combination between events tending to the same shear regions will lead to coupled events in that shear region, while events tending to different shear regions will meet in the middle.

## 8.2 Turbulence

The turbulent energy budget has been calculated to further the understanding of this flow. The formulas used are specified in Section D. The results are considered near the interface ( $y^+ < 100$ ) in Figs. 8.16 and 8.17. Comparing the results to the turbulent energies described by [8], the production is very similar in shape. Even the detail that the production on the gas side becomes virtually zero slightly above the interface, while the production on the liquid side only becomes zero at the interface itself, is in agreement. The turbulent diffusion is also very similar, both in general shape and in the sign changes near the interface. Also the viscous diffusion and the turbulent dissipation show good agreement. The only clear difference comes from the pressure diffusion.

It is seen that the pressure diffusion is not present in the bottom fluid. This is not so strange, there is no pressure gradient or other form of pressure influencing the flow, therefore there is also no pressure diffusion. On the other hand, the gas shows a rather different pressure diffusion than what has been described in [8]. There, the pressure diffusion was barely visible near the interface and nowhere away from the interface, while in the gas in this simulation, it's larger than the magnitude of the production. An explanation has not been found and will require further analysis.

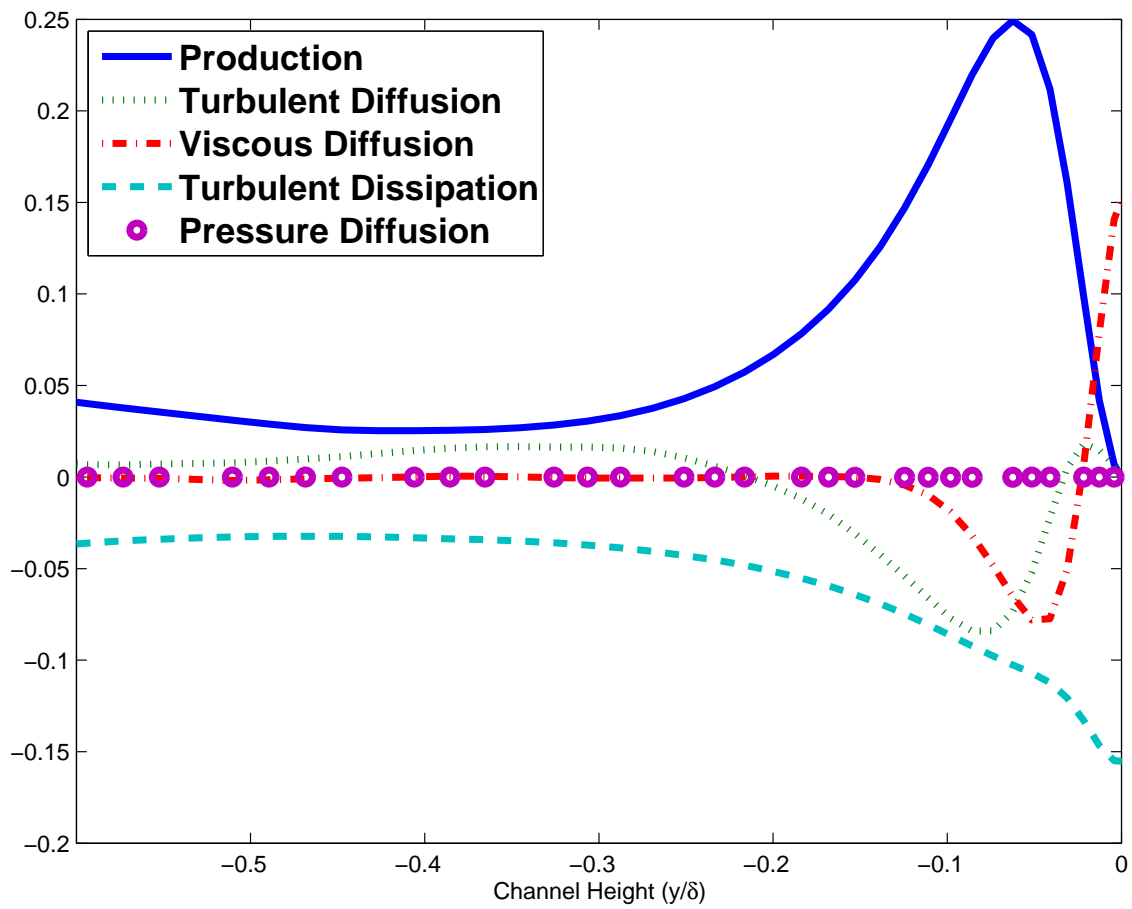


Fig. 8.16: Components of the turbulence on the liquid side of the interface

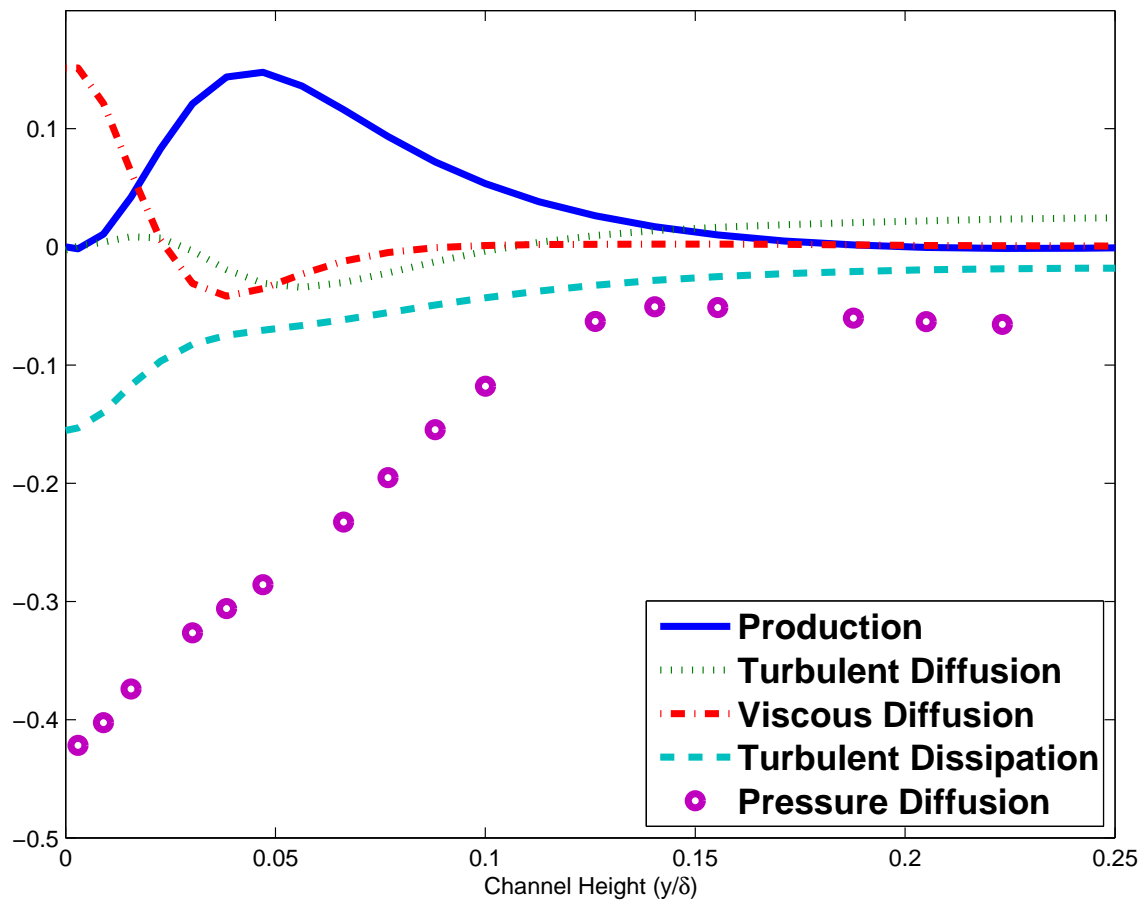


Fig. 8.17: Components of the turbulence on the gas side of the interface

## CHAPTER 9

# CONCLUSION

---

In this thesis, a viscous coupling has been successfully applied to the LES model. This has been verified through comparison to analytical flows and analysis of the accuracy of the model.

The application of this model to three dimensions has been done as the logical next step, allowing for analysis of a turbulent channel flow with two fluids. The flow was similar to air over water, where it was seen that the turbulence was strongest in the region 60 to 90 nondimensional units above the interface.

The most thorough research has been applied to the turbulence near the interface. Here it was found that in the gas, as expected, ejections and sweeps dominate over respectively low and high shear stress regions, but that in the liquid, first and third quadrant events have this same distinction.

An explanation is given by comparing these results to previous research, where there was a pressure gradient in the liquid and no distinction was found. The liquid tends to these first and third quadrant events, while a pressure gradient leads to ejections and sweeps.

In the simultaneous occurrence of events on both sides of the interface, an event was found about sixty percent of the time. These coupled events showed a strong tendency for first and third type of events on the gas side to be coupled with the same type on the liquid side. On the other hand, events of the second and fourth type on the liquid side showed the same strong tendency with the same type of events on the gas side. Therefore, the least common event types are almost always associated with the same event type on the other side, despite the normal direction being opposite.

These conclusions yield insight into the behaviour of turbulence near an interface, setting expectations for further experiments and showing the importance of further research in this area.



# CHAPTER 10

## DISCUSSION

---

There is still a lot of room for further research. The conclusions from the previous chapter are tangible, but require more referencing results. In addition to these results, there is the suspicion that due to the nature of coupled events near the interface, streamwise vortices are present. It was found that the events are most often pointed in the opposite normal direction, something which would also be the case if these streamwise vortices are indeed present.

To improve the current model, the assumption that the interface is flat should be reevaluated, as well as the accuracy of this coupling and the behaviour of the pressure. Making the model more realistic, firmly second-order accurate again and in accordance with the expectancy for the pressure, will lead to the robustness needed for further application. Then, there will be a lot of possibility for doing more analysis of two-fluid flows, both looking at more theoretical flows with more disparate Reynolds numbers as well as flows with other different properties, like the bounding walls and the pressure gradients. On the other hand, it can also be applied to more realistic flows, looking more closely at the behaviour of, for example, open sea.

Finally, the underlying code is still based on a single computer and needs to be adapted to work with, for example, message passing interface (MPI), so it can be used on supercomputers.



# Bibliography

- [1] M. R. Ansari and B. Arzandi. Two-phase gas-liquid flow regimes for smooth and ribbed rectangular ducts. *International Journal of Multiphase Flow*, 38(1):118–125, 2012.
- [2] V. Armenio and U. Piomelli. Lagrangian mixed subgrid-scale model in generalized coordinates. *Flow, Turbulence and Combustion*, 65(1):51–81, 2001.
- [3] M. Fulgosi, D. Lakehal, S. Banerjee, and V. De Angelis. Direct numerical simulation of turbulence in a sheared air-water flow with a deformable interface. *Journal of Fluid Mechanics*, (482):319–345, 2003.
- [4] J. C. R. Hunt, D. D. Stretch, and S. E. Belcher. Viscous coupling of shear-free turbulence across nearly flat fluid interfaces. *Journal of Fluid Mechanics*, 671:96–120, 2011.
- [5] J. Kim and P. Moin. Application of a fractional-step method to incompressible navier-stokes equations. *Journal of Computational Physics*, 59(2):308–323, 1985.
- [6] J. Kim, P. Moin, and R. Moser. Turbulence statistics in fully developed channel flow at low reynolds number. *Journal of Fluid Mechanics*, 177:133–166, 1987.
- [7] K. Lam and S. Banerjee. Investigation of turbulent flow bounded by a wall and a free surface. In *American Society of Mechanical Engineers, Fluids Engineering Division (Publication) FED*, volume 72, pages 29–38, 1988.
- [8] P. Lombardi, V. De Angelis, and S. Banerjee. Direct numerical simulation of near-interface turbulence in coupled gas-liquid flow. *Physics of Fluids*, 8(6):1643–1665, 1996.
- [9] D. Yang and L. Shen. Simulation of viscous flows with undulatory boundaries: Part ii. coupling with other solvers for two-fluid computations. *Journal of Computational Physics*, 230(14):5510–5531, 2011.
- [10] Y. Zang, R. L. Street, and J. R. Koseff. A non-staggered grid, fractional step method for time-dependent incompressible navier-stokes equations in curvilinear coordinates. *Journal of Computational Physics*, 114(1):18–33, 1994.



# APPENDIX A

## NOTATION

---

What is mentioned here is the same throughout the paper, unless mentioned otherwise. Subscripts are indicated to differ between the top and the bottom fluids, usually with the numbers 1 and 2 respectively, though sometimes with  $t$ ,  $b$ ,  $top$  or  $bottom$  for clarity.

The grid is a non-staggered grid as described in [10]. A schematic view of such a 2d-grid, stretched in the  $y$ -direction, is given in Fig. A.1. The dots are the locations where the velocities and the pressure are defined. The contravariant velocities are defined on the cell faces.

$1 - 1$	A coupled event, the first number indicates the event in the top fluid, the second number the bottom fluid
$A$	Amplitude used in the Stokes oscillating plate
$a$	Coefficient used in the interface boundary condition
$b$	Coefficient used in the interface boundary condition
$c$	Coefficient used in the interface boundary condition
$c_{ij}$	A coupled event of type $i - j$
$D_k$	The viscous diffusion, part of $Dk/Dt$
$e$	An event
$F_{ij}$	Cumulative distribution function for a coupled event $i - j$
$h$	Characteristic length of the flow in the $y$ -direction
$h_0$	$y$ -value of the bottom boundary in a domain
$h_1$	$y$ -value of the top boundary in a domain
$k$	Turbulent kinetic energy budget
$Dk/Dt$	Material derivative of the turbulent kinetic energy budget
$L$	The characteristic length of a flow
$N_x$	Number of grid cells in the $x$ -direction
$N(t)$	Number of flow fields in the temporal direction
$P_k$	The production, part of $Dk/Dt$
$P_q$	Probability of an event of type $q$ happening over a certain area of shear stress
$\partial p/\partial x$	The pressure gradient, a constant
$q_i$	Event of type $i$
$R_{uu}$	Spatial correlation between the two indicated velocities
$Re$	The Reynolds number
$Re_w$	The boundary Reynolds number
$T_k$	The turbulent diffusion, part of $Dk/Dt$
$U(j)$	The mean velocity at a certain point in the $y$ -direction
$u'_{rms}$	The root mean square of the velocity

$u'$	The perturbation from the average velocity
$u_\tau$	The shear velocity
$u^*$	Predictor for $u^{n+1}$ in the predictor-corrector scheme
$u_1$	The velocity in the streamwise direction for the top fluid
$u_2$	The velocity in the streamwise direction for the bottom fluid
$v_1$	The velocity in the normal direction for the top fluid
$v_2$	The velocity in the normal direction for the bottom fluid
$w_1$	The velocity in the spanwise direction for the top fluid
$w_2$	The velocity in the spanwise direction for the bottom fluid
$x$	The streamwise direction
$y$	The wall-normal direction
$y^+$	Nondimensional wall distance
$z$	The spanwise direction
$\Delta t$	Time step in scheme discretization
$\Delta x$	Spatial difference in scheme discretization
$\Delta^1 y$	Distance between the grid point at the interface and the closest grid point in the $y$ -direction, relative to the first grid cell.
$\Delta^2 y$	Distance between the grid point at the interface and the second closest grid point in the $y$ -direction, relative to the first grid cell.
$\delta$	Used for normalisation of the $y$ -domain to $[-1, 1]$
$\epsilon_k$	The turbulent dissipation, part of $Dk/Dt$
$\kappa_s$	Characteristic roughness length scale
$\mu$	The dynamic viscosity
$\nu$	The kinematic viscosity
$\Pi$	The pressure gradient, a constant
$\Pi_k$	The pressure diffusion, part of $Dk/Dt$
$\rho$	The density
$\sigma_{c_{ij}}$	Total stress present in a coupled event $c_{ij}$
$\tau$	The shear stress
$\tau_w$	The wall shear stress
$\tau_y$	The interfacial shear stress
$\tau_{xy}$	Component of the interfacial shear stress
$\tau_{yz}$	Component of the interfacial shear stress
$\Phi_k$	The pressure strain, part of $Dk/Dt$
$\phi_\tau$	Indicator used in the calculation of the cumulative distribution function $F_{ij}$
$\psi$	Weight used to account for the non-uniformity of the velocity locations
$\omega$	Frequency used in the Stokes oscillating plate

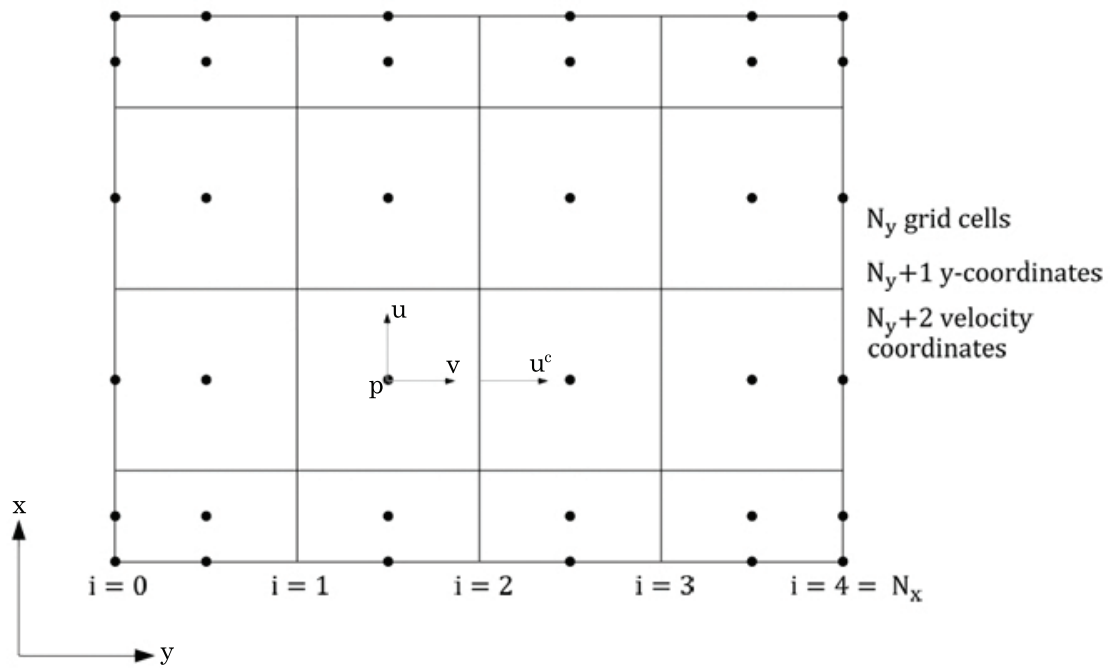


Fig. A.1: Schematic grid

Normalisation of variables, indicated by a plus sign:

$$\begin{aligned}
 u_\tau &= \sqrt{\frac{\tau_{int}}{\rho}} \\
 y^+ &= \frac{u_\tau y}{\nu} = Re \cdot y \\
 t^+ &= t \frac{u_\tau^2}{\nu} \\
 \bar{u}^+ &= \bar{u} / u_\tau \\
 u_{rms}^+ &= \frac{\sqrt{u'^2}}{u_\tau} \\
 u'v'^+ &= \frac{\overline{u'v'}}{u_\tau^2} \\
 \frac{Dk^+}{Dt} &= \frac{Dk^+}{Dt} \frac{\nu}{u_\tau^4}
 \end{aligned}$$



## APPENDIX B

# SPATIAL AND TEMPORAL CORRELATION

---

Considering that instantaneous flow fields do not contain all available information in a turbulent flow, statistics will need to be applied to get meaningful results. The first assumption in these statistics is that one is dealing with identically distributed and independent events. These events are the instantaneous flow fields. To guarantee the independence, the correlation between flow fields needs to be analysed, the so-called autocorrelation. Between subsequent iterations there is a high correlation (near one), while, for a flow field far away temporally, the sought correlation should be sufficiently close to zero. While the precise shape of the flow is independent after a sufficiently long time, the form of the flow will still remain similar to the average form of the flow. In other words, the correlation between two flow fields will not converge to zero in time. Therefore, to be able to say that there is no correlation between two flow fields, math is required. The specific formula for autocorrelation of a temporal distance  $\tau$  is:

$$\frac{\mathbb{E}[(U(j, t) - U(j))(U(j, t + \tau) - U(j))]}{\sigma^2} \quad (\text{B.1})$$

This formula is assuming that the process has a time-independent mean and variance, which is satisfied if the process is in a steady state. Written out this becomes:

$$\frac{\frac{1}{N(t-\tau)} \sum_{t=1}^{N(t-\tau)} (U(j, t) - U(j))(U(j, t + \tau) - U(j))}{\frac{1}{N(t)} \sum_{t=1}^{N(t)} (U(j, t) - U(j))^2} \quad (\text{B.2})$$

$N$  is the number of flow fields evaluated in the time indicated by the argument. The velocity  $u$  here is the velocity averaged over the streamwise and spanwise direction at a certain height. Looking closely at this formula, one sees that the magnitude of the correlation considered, will become less as the number of events increases. This is because the sum in the numerator will not become significantly larger, as the terms added are equally positive and negative over the long run. The count of the number of events does increase, making the numerator decrease overall.

To get a good idea of the time distance at which the direct correlation from the previous iteration is not of influence anymore, one needs to look at the system at a few critical points, for behaviour varies in different parts of the flow. Therefore, the boundary layer and the inner region of the top fluid are of interest. If the bottom fluid is very viscous, the lack of turbulence will keep the autocorrelation high, which needs to be taken into account for the bottom fluid.

The spatial correlation is a good tool to analyse the connectedness in the flow itself. For that, the following formula has been used:

$$R_{uu}(y) = \frac{\overline{(u(y_1) - \overline{u(y_1)}) (u(y) - \overline{u(y)})}}{\sqrt{\overline{(u(y_1) - \overline{u(y_1)})^2} \overline{(u(y) - \overline{u(y)})^2}}} \quad (\text{B.3})$$

With  $y_1$  the point of which the spatial correlation is considered.

## APPENDIX C

# TURBULENCE STATISTICS

---

In processing the results, a lot of mathematics, especially from the field of probability and statistics, need to be applied correctly.

To calculate the mean velocity profile over the height, the average is taken over the stream-wise, spanwise and temporal direction, providing the average  $U(j)$  as a function of the height.

$$U(j) = \frac{1}{N(t)} \frac{1}{N_x + 1} \frac{1}{N_z} \sum_{t=1}^{N(t)} \sum_{i=0}^{N_x+1} \sum_{k=1}^{N_z} \psi(i) u(i, j, k, t), j \in (0, N_y + 2) \quad (\text{C.1})$$

$$\psi(i) = \begin{cases} 1, i \in (1, N_x) \\ \frac{1}{2}, i=0 \text{ or } i=N_x+1 \end{cases} \quad (\text{C.2})$$

$$(\text{C.3})$$

Here  $\psi$  is a weight introduced to incorporate the fact the grid is not equidistant at the boundaries.

Using this average, the root mean square velocity can be calculated, which is basically the variance of the variable.

$$u'_{rms}(j) = \sqrt{\left| U(j)^2 - \frac{1}{N(t)} \frac{1}{N_x} \frac{1}{N_z} \sum_{t=1}^{N(t)} \sum_{i=1}^{N_x} \sum_{k=1}^{N_z} u(i, j, k, t)^2 \right|} \quad (\text{C.4})$$

The sums do not contain the boundary (which has variance zero), so there is no need for weights to be applied. For the velocities  $v$  and  $w$ , the above equations are performed in the same way. With this, the basic second-order statistics of a turbulent flow are known.

To analyse the behaviour of turbulence at the interface, events have been defined, as well as the shear stress at the interface.

At five points above and below the interface, respectively  $y^+ = 1.06, 3.26, 5.62, 8.16, 10.88$  and  $y^+ = 1.04, 3.18, 5.43, 7.79, 10.27$ , the values of  $u'$  and  $v'$  are determined. The definition in these calculations of  $u'$  is the difference between the value in the point and the average value of  $u$  at that height in that timewindow,  $U(j, t)$ . For  $v'$  it's the same, except  $v'$  is oriented away from the interface.

$$u'(i, j, k, t) = u(i, j, k, t) - U(j, t) \quad (\text{C.5})$$

$$v'(i, j, k, t) = \begin{cases} v(i, j, k, t) - V(j, t), & \text{if } j > N_y/2 + 1 \\ V(j, t) - v(i, j, k, t), & \text{otherwise} \end{cases} \quad (\text{C.6})$$

Quadrants can then be defined properly. The first quadrant, when  $u' > 0$  and  $v' > 0$ , is high-speed fluid motion, directed away from the interface. The second quadrant is when  $u' < 0$  and  $v' > 0$  are called ejections and contains low-speed fluid moving away from the interface. The third quadrant,  $u' < 0$  and  $v' < 0$ , is comprised of low-speed fluid moving to the interface. Finally, the fourth quadrant,  $u' > 0$  and  $v' < 0$ , are called sweeps and contain high-speed fluids directed towards the interface. For the liquid, it is important to keep in mind  $v'$  is oriented away from the interface.

If in four out of the five measurement points in one fluid, the same quadrant is present, it is an event. For an event, three things are recorded: the type of event ( $q_1, q_2, q_3, q_4$ ), the total Reynolds stress in the event ( $\sum u'v'$ ) and the average Reynolds stress in the event ( $\overline{\sum u'v'}$ ). So, if at four of the five points there is a sweep event ( $q_2$ ) with an average Reynolds stress of 1 and an ejection ( $q_4$ ) with a value of -1 at the fifth point, the total strength ( $\sum u'v'$ ) is 4. The average stress ( $\overline{\sum u'v'}$ ) of this event is 1, the same as it would be if the ejection was a sweep with value 1.

These events are then sorted by the shear stress at the interface at the corresponding  $(\hat{x}, \hat{z})$ -coordinates. The total interfacial shear stress is defined as:

$$\tau_y = (\tau_{xy}^2 + \tau_{yz}^2)^{\frac{1}{2}} \quad (\text{C.7})$$

With

$$\tau_{xy} = \mu \left( \frac{\partial u}{\partial y} + \frac{\partial v}{\partial x} \right) \quad (\text{C.8})$$

$$\tau_{yz} = \mu \left( \frac{\partial w}{\partial y} + \frac{\partial v}{\partial z} \right) \quad (\text{C.9})$$

This shear stress has then been normalised by the maximum interfacial shear stress found in the simulation:

$$\tau_y = \frac{\tau_y}{\max_{x,z,t} \tau_y} \quad (\text{C.10})$$

For the probability function in Figs. 8.10 and 8.11, the probability has been calculated by classifying the normalised interfacial shear stress in bands of width 0.02. Additionally, the probabilities are based on the number of events, not on the stress in those events. That means that the probability  $P$  for an event of a certain type  $q_i$  is dependent on the amount of events that are present of that type in each band ( $e(\tau_y; q_i)$ ), divided by the total number of events  $N_e$ .

$$P_{q_i}(\tau_y) = \frac{1}{N_e} \sum_{N_e} e(\tau_y; q_i) \quad (\text{C.11})$$

The bands are indicated by  $\tau_y$ . The full definition of whether there is an event is given by:

$$e(\tau_y; q_i) = \begin{cases} 1 & \text{if the event corresponding to shear stress band } \tau_y \text{ is of type } q_i \\ 0 & \text{otherwise} \end{cases} \quad (\text{C.12})$$

The cumulative distribution functions (Figs. 8.12 and 8.13), on the other hand, are based on the total shear of the coupled event,  $c_{ij}$ . It is built up by sorting all the coupled events based on their interfacial shear stress. For the value of the cumulative distribution function at shear stress equal to 0, the cumulative distribution function for a certain coupled event i-j ( $F_{ij}$ ) is the sum over all events with more stress than 0, of the total stress for that event, divided by the total stress present in all the coupled events. Then, the same calculation is done for the next smallest interfacial shear stress ( $x_\tau$ ). The numerator contains all coupled events which have  $\tau_c > x_\tau$ , with  $\tau_c$  the stress corresponding to a coupled event. Written down as a formula, that becomes:

$$F_{ij}(x_\tau) = \frac{\sum_{N_c} \sigma_{c_{ij}}}{\sum_{N_c} \tau_c} \quad (\text{C.13})$$

$\sigma_{c_{ij}}$  is the total stress present in a coupled event of the combination i-j, where the interface has more than or equal stress to  $x_\tau$ .

$$\sigma_{c_{ij}} = \sum_{c_{ij}} \phi_\tau \sum_{y^+} u'v' \quad (\text{C.14})$$

$$\phi_\tau = \begin{cases} 1 & \text{if } \tau_c > x_\tau \\ 0 & \text{otherwise} \end{cases} \quad (\text{C.15})$$

From coupled events, the analysis is extended to include only strong coupled events. These are events which have a total Reynolds stress bigger than a certain treshold. This will remove the very weak but plentiful events from the overall results.

$$\sum u'v' > 1.75 \overline{\sum u'v'} \quad (\text{C.16})$$

In words, this formula says that an event in which in four of five points contains less stress than 1.75 points do on average, they are not counted as events.



## APPENDIX D

# TURBULENT KINETIC ENERGY

---

The definition of the turbulent kinetic energy budget,  $k$ , is defined by the fluctuations present in the system.

$$k = \left( \overline{u'^2} + \overline{v'^2} + \overline{w'^2} \right) \quad (\text{D.1})$$

The energy can however be better described by looking at the material derivative of the kinetic energy.

$$\frac{Dk}{Dt} = \frac{\partial k}{\partial t} + u \frac{\partial k}{\partial x} + v \frac{\partial k}{\partial y} + w \frac{\partial k}{\partial z} \quad (\text{D.2})$$

$$= P_k + \Pi_k + T_k + \Phi_k + D_k + \epsilon_k \quad (\text{D.3})$$

With  $P_k$  the production,

$$P_k = -\overline{u'_i u'_j \frac{\partial \overline{u}_i}{\partial x_j}} \quad (\text{D.4})$$

$\Pi_k$  the pressure diffusion,

$$\Pi_k = -\frac{1}{\rho} \overline{\frac{\partial p'}{\partial x_i} u'_i} \quad (\text{D.5})$$

$T_k$  the turbulent diffusion,

$$T_k = -\frac{1}{2} \overline{\frac{\partial u'_i u'_i u'_j}{\partial x_j}} \quad (\text{D.6})$$

$\Phi_k$  the pressure strain,

$$\Phi_k = \frac{1}{\rho} \overline{p' \frac{\partial u'_i}{\partial x_j}} \quad (\text{D.7})$$

$D_k$  the viscous diffusion,

$$D_k = \frac{1}{2Re} \overline{\frac{\partial^2 u'_i u'_i}{\partial x_j \partial x_j}} \quad (\text{D.8})$$

and  $\epsilon_k$  the turbulent dissipation,

$$\epsilon_k = -\frac{1}{Re} \overline{\frac{\partial u'_i}{\partial x_j} \frac{\partial u'_i}{\partial x_j}} \quad (\text{D.9})$$

It should be noted that due to the incompressibility of the flow,  $\Phi_k$  is equal to zero.

These different parts of the turbulence are relevant along the normal direction, so the averages indicated here need to be taken carefully. The method used is explained by the following example.

$$\begin{aligned} P_k &= -\overline{u'_i u'_j} \frac{\partial \bar{u}_i}{\partial x_j} \\ &= -\left( \overline{u'v'} \frac{\partial \bar{u}}{\partial y} + \overline{u'w'} \frac{\partial \bar{u}}{\partial z} + \overline{v'w'} \frac{\partial \bar{v}}{\partial z} \right. \\ &\quad \left. + \overline{v'u'} \frac{\partial \bar{v}}{\partial x} + \overline{w'u'} \frac{\partial \bar{w}}{\partial x} + \overline{w'v'} \frac{\partial \bar{w}}{\partial y} \right. \\ &\quad \left. + \overline{u'u'} \frac{\partial \bar{u}}{\partial x} + \overline{v'v'} \frac{\partial \bar{v}}{\partial y} + \overline{w'w'} \frac{\partial \bar{w}}{\partial z} \right) \end{aligned}$$

Then, a term is handled by averaging where it is required beforehand and averaging where needed to give results along the normal direction.

$$\overline{u'w'} \frac{\partial \bar{u}}{\partial z} = \frac{1}{N_x N_z N_t} \sum_{i,k,\tau} (u'w') \frac{1}{N_z} \sum_k \left( \frac{\partial}{\partial z} \left( \frac{1}{(N_x N_t)} \sum_{i,\tau} u \right) \right)$$

The linearity of the derivative allows variations on this, as long as one takes the appropriate derivative in a direction before averaging in that direction.